https://doi.org/10.5194/egusphere-2026-3143
Preprint. Discussion started: 24 June 2026

Vertical Structure and Evolution of the Stratus-to-Fog-to-Stratus Transition: first high-resolution UAV-LCPIS Measurements over the Yellow Sea coast

Qingwei Zeng[1,2], Lei Liu[1,2,*], Lele Cai[1], Hao Zhou[1,2], Qinghui Li[1,2], Xichuan Liu[1,2]

[1]College of Meteorology and Oceanography, National University of Defense Technology, Changsha, China
[2]Key Laboratory of High Impact Weather (special), China Meteorological Administration, Changsha, China

Correspondence to: Lei Liu (liulei17c@nudt.edu.cn).

Abstract. This study presents, for the first time, high-resolution concurrent vertical profiles of temperature, humidity, water vapour, and fog/cloud droplet microphysics during a stratus-fog-stratus transition over the Yellow Sea (15-16 May 2025). The primary observational platform relied on a novel Lightweight Cloud Particle Imager sonde (LCPIS) deployed on an unmanned aerial vehicle (UAV) system. The event progressed through three distinct stages: pre-fog stratus, dense fog (minimum visibility ~100 m), and lifting to stratus. Pre-fog stratus featured a shallow mixed layer ($Ri < 0.25$) capped by a strong inversion ($Ri > 0.25$), trapping moisture below 300 m. During the fog transition, the inversion base stabilized at 270 m with a lapse rate of 5.0 $°\mathrm{C}\cdot(100\,\mathrm{m})^{-1}$, while the saturated layer extended to the surface. Within the fog layer, the Richardson number (Ri) was negative, indicating vigorous turbulent mixing, while $Ri > 0.25$ near the fog top formed a dynamically stable cap. After dissipation, Ri turned positive and evaporated moisture re-formed stratus. Peak droplet number concentration (NC) increased from 50-100 cm^{-3} (pre-fog) to 100-120 cm^{-3} (fog), liquid water content (LWC) doubled from 0.1-0.2 to 0.2-0.45 cm^{-3}, and mean diameter ranged 10-20 μm. Microphysical peaks occurred at ~200 m in both pre-fog and fog stages. Key transition indicators include downward extension of the saturated layer to the surface, rise of the zero dew-point depression height, and NC stabilization with LWC increase. This study provides the first synchronized vertical observations of thermodynamic, water vapour and microphysical parameters during a stratus-fog-stratus transition, offering a robust observational basis for improving sea fog forecasting.

1 Introduction

Sea fog is a pervasive meteorological phenomenon that drastically reduces horizontal visibility, posing significant risks to maritime navigation, coastal fisheries, and aviation safety (Torregrosa et al., 2014; Gultepe et al., 2019; Taylor et al., 2021; Fernando et al., 2025). Despite its socio-economic importance, predicting the sea fog lifecycle-specifically the bidirectional transition between stratus and fog-remains a major challenge for numerical weather prediction (NWP) models (Costabloz et al., 2025; Fernando et al., 2025). A primary limiting factor is the scarcity of high-resolution vertical profiles capable of resolving the tight coupling among microphysics, turbulence, and thermodynamics within the marine atmospheric boundary layer (MABL).

https://doi.org/10.5194/egusphere-2026-3143
Preprint. Discussion started: 24 June 2026

A prevalent mechanism for sea fog formation is cloud-base lowering (CBL, also referred to as stratus lowering), which has been frequently documented across various coastal and open-ocean regions (Goodman, 1977; Fu et al., 2008; Koračin et al., 2014; Dorman et al., 2021; Pope and Igel, 2025). The underlying physical mechanisms driving CBL exhibit significant regional variability. Off the California coast, stratus lowering is primarily driven by cloud-top radiative cooling and large-scale subsidence (Koračin et al., 2001; Lewis et al., 2004; Oliver et al., 1978; Pilié et al., 1979). In the Grand Banks of Newfoundland, top-down convection, droplet sedimentation and evaporative cooling play a dominant role (Singh et al., 2024). Along the Atlantic coast of Western Europe, advection of cold-moist air over warmer seas combined with nocturnal cooling is the main driver (Gultepe et al., 2007). Beyond these localized drivers, the vertical evolution of the stratus-fog system is characterized by complex temporal dynamics, as the transition is often cyclical rather than unidirectional; for instance, fog frequently lifts into low-level clouds during the daytime and reforms at night (Yang et al., 2021).

Despite these regional insights, direct observations of the vertical MABL structure during such transitions remain limited. This knowledge gap is significant because the governing processes (such as radiative cooling, turbulent mixing, droplet sedimentation, and entrainment) occur throughout the entire depth of the MABL. While various sea fog detection techniques have been developed, each presents specific advantages and limitations. In situ surface-based microphysical measurements are generally limited to single-point observations, thus precluding the acquisition of vertical profiles (Ming et al., 2019). Remote sensing instruments (lidar, cloud radar) suffer from near-surface blind zones, typically missing the lowest 100 m where fog forms (Fernando et al., 2021). Meteorological towers are vertically constrained (< 100 m), and tethered balloons are highly sensitive to wind speeds (where speeds $> 5\ \mathrm{m \cdot s^{-1}}$ restrict deployment) (Egli et al., 2015; Price et al., 2015; Ramelli et al., 2020). Although multi-rotor UAVs are capable of profiling the MABL, their restricted payload capacity (< 5 kg) typically precludes the deployment of conventional instruments such as the Cloud Droplet Probe (CDP) (Fuchs et al., 2025). More critically, most available lightweight cloud probes function as offline data loggers, lacking real-time telemetry links. This absence of live feedback prevents researchers from monitoring the instrument's operational status or identifying the exact moment of cloud-base penetration in situ (Girdwood et al., 2020; Kaikkonen et al., 2024; Chambers et al., 2024). Consequently, synchronous vertical profiles of thermodynamic and microphysical variables are almost non-existent, limiting current understanding to qualitative descriptions and hindering model refinement (Gultepe et al., 2007; Fernando et al., 2021; Costabloz et al., 2025).

In this study, we examine in situ microphysical and thermodynamic measurements acquired by a newly developed Lightweight Cloud Particle Imager Sonde (LCPIS) mounted on an unmanned aerial vehicle (UAV) during a sea fog event along the Yellow Sea coast (15-16 May 2025). These observations provide, for the first time, a quantitative characterization of the vertical evolution of microphysical properties during the stratus-fog-stratus transition, from the pre-fog stratus stage through the development and maintenance of dense fog, and to the final dissipation phase as the fog elevates back into stratus. By combining these high-resolution vertical profiles with surface observations, reanalysis data, radiosonde profiles, cloud radar scans and satellite imagery, we elucidate the coupled microphysical, thermodynamic and dynamic mechanisms governing the transition. Emphasis is placed on the role of turbulent mixing, the Richardson number structure, and cloud-top entrainment. This study offers novel observational insights and a robust observational data basis for improving sea-fog parameterizations and forecasts in the Yellow Sea region.

The remainder of this paper is organized as follows: Section 2 details the design principles, performance calibration, and data processing algorithms of the LCPIS. Section 3 presents the macroscopic and vertical structure evolution during the transition, emphasizing the vertical profiles of thermodynamic, dynamic, and microphysical parameters. Section 4 discusses the transition mechanisms and proposes a conceptual model, while also validating the LCPIS performance. Finally, Section 5 summarizes the primary conclusions.

2 Instrument and method

2.1 Experimental site and instruments

The data analysed in this study were obtained during the Yellow Sea and Bohai Sea Fog Scientific Observation Experiment. The Yellow Sea is a key area of high sea-fog frequency along the eastern coast of China. From April to July, advection-cooling fog accounts for over 70% of the total annual fog days (Guo et al., 2021; Liu et al., 2021; Wan et al., 2020). Accordingly, annual field campaigns are conducted from April to July to document the complete life cycle of sea fog from inception through development to maintenance and dissipation. The primary observation site is located at the Huangdao Meteorological Bureau, Qingdao (35.83° N, 120.03° E; 76m above sea level, a.s.l.). Situated adjacent to the Yellow Sea coastline, this station is positioned within the central region of frequent fog events across the Yellow and Bohai Seas. It serves as a critical observatory for continuous sea fog monitoring. The prevailing meteorological conditions at this site are representative of the broader coastal marine environment in the Yellow Sea. The specific sea fog case analysed in this study was recorded from 15 to 16 May 2025. All times cited in this paper are in Coordinated Universal Time (UTC).

Figure 1 depicts the observation site and instrumentation layout. As shown in Fig. 1a, the unobstructed terrain minimizes local aerodynamic disturbances, ensuring that vertical profiles accurately reflect the characteristics of the undisturbed marine boundary layer (MABL). The primary instrumentation deployed includes an automatic weather station, a ground-based droplet spectrometer (LCPI), a visibility meter, a Ka-band cloud radar, and the LCPIS. The LCPI was also developed by our research group and shares its detection principle with the LCPIS. Both utilize forward-scattering, microscopic-imaging technology to acquire high-definition images of hydrometeors, applying image-processing algorithms for particle identification, size retrieval, and number-concentration calculation. The LCPI was cross-validated against a fog monitor (FM-120, Droplet Measurement Technologies Inc., USA) during an intercomparison campaign at the Mount Lushan Cloud and Fog Observatory. The results demonstrated high consistency in droplet number concentration and size distribution, confirming its reliability (Cai et al., 2024). As indicated in Fig. 1b, the LCPI was installed in the northeastern corner of the observation site (red dashed box in Fig. 1a), while the Ka-band cloud radar was positioned in the western area (yellow box, Fig. 1c). UAV profiling was conducted in the area marked by the blue dashed box. The UAV employed was a DJI Matrice 350 RTK quadcopter, which features a maximum flight time of 55 min and a payload capacity of 2.5 kg. To mitigate potential sampling distortions and measurement biases induced by rotor-wash-generated turbulence, the LCPIS was suspended 20 m below the UAV airframe via a lightweight flexible cable (Fig. 1d). This configuration ensures the instrument intake probes a stable, unaffected ambient environment, thereby maintaining the fidelity of the airborne measurements. Fig. 1e provides a close-up view of the LCPIS probe during pre-deployment battery charging.

Figure 1. Experimental setup at the Huangdao observation site. (a) Aerial view; (b) ground-based droplet spectrometer and visibility sensor; (c) Ka-band cloud radar; (d) UAV during flight; (e) LCPIS probe close-up.

2.2 Lightweight Cloud Particle Imager Sonde

2.2.1 Instrument design

The LCPIS is a compact, highly integrated instrument designed to provide the operational utility of conventional radiosondes. Its external configuration is shown in Fig. 2a. The dimensions of the LCPIS are 320 mm×220 mm×180 mm. The housing is constructed from high-density, 3D-printed foam to maintain a total mass about 1.5 kg. The primary function of the LCPIS is to acquire two-dimensional images of cloud particles to derive morphological parameters, including size and shape. Additionally, the LCPIS incorporates a combined temperature and humidity sensor, a high-precision water vapour absorption cell, and a BeiDou positioning module. The temperature and humidity sensors are derived from operational GTS type radiosondes. These components protrude from the side of the housing to facilitate direct contact with the ambient flow. The water vapour assembly utilizes tunable diode laser absorption spectroscopy (TDLAS), governed by the Beer–Lambert law:

$$I = I_0 \cdot e^{-\alpha(\lambda)\cdot VMR\cdot L} \tag{1}$$

https://doi.org/10.5194/egusphere-2026-3143
Preprint. Discussion started: 24 June 2026

where I_0 represents the incident laser intensity prior to passing through the sample, I is the transmitted intensity after interaction with water vapour, $\alpha(\lambda)$ is the absorption coefficient of water vapour molecules at a specific wavelength λ, VMR is the volume mixing ratio of water vapour, and L is the effective optical path length. In this configuration, a semiconductor laser beam traverses an absorption cell with a fixed length of L=14 cm. The beam undergoes attenuation due to selective absorption by water vapour molecules, which is then detected by a photodetector. The water vapour VMR is typically retrieved in units of parts per million (ppm) or parts per billion (ppb). For atmospheric applications, the VMR is converted to water vapour content (q, in g·m^{-3}), representing the water vapour mass per unit volume of moist air. The conversion is defined as follows:

$$q = VMR \times \frac{P \times M_{H_2O}}{R \times T} \tag{2}$$

where q is the water vapour content (g·m^{-3}), P is the ambient pressure (Pa), T is the absolute temperature (K), $M_{H_2O} = 18.016$ g/mol is the molar mass of water vapour, and R=8.314 Pa·m³/(mol·K) is the universal gas constant. The internal positioning module operates at 1575.42 MHz, providing real-time spatial coordinates. Power is supplied by a low-temperature lithium battery pack (3S2P configuration) with a total capacity of 5 Ah (Fig. 2d).

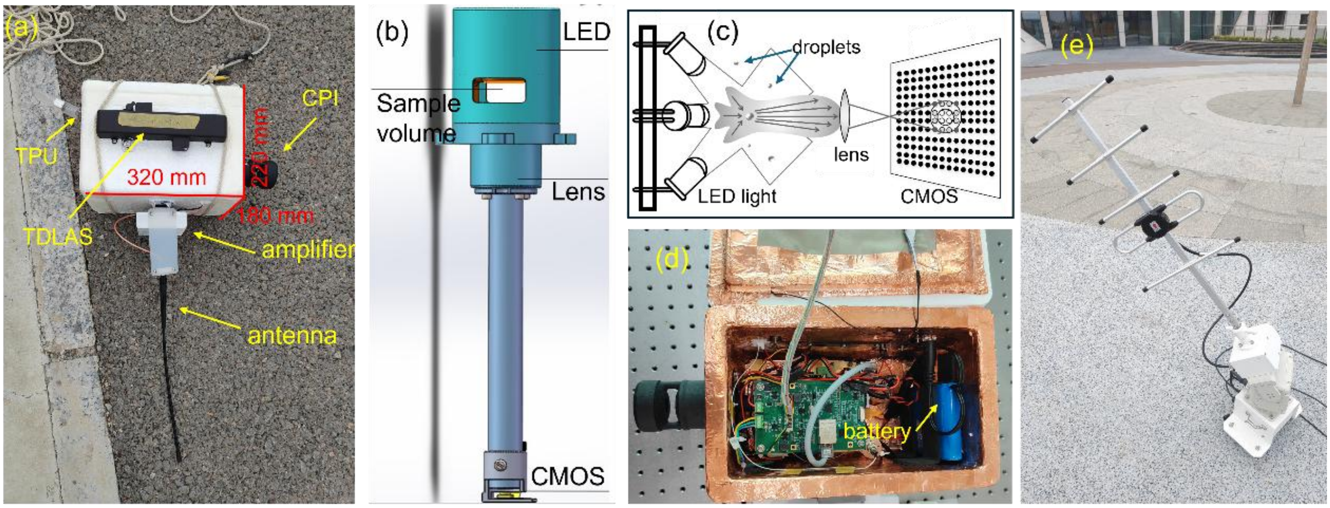

Figure 2. Instrumental design and measurement principle of the Lightweight Cloud Particle Imager sonde (LCPIS): (a) external housing and configuration; (b) internal structural schematic; (c) optical pathway for particle imaging; (d) internal component layout; and (e) ground-based receiving antenna.

The cloud-particle imaging unit assembly constitutes the core component of the LCPIS. It consists of a CMOS sensor, a microscopic objective lens, and a light source assembly (Fig. 2b). The housing is 3D-printed from black nylon to simultaneously provide structural rigidity and weight reduction. The measurement principle is analogous to that of ground-based imaging spectrometers LCPI. As shown in Fig. 2c, an annular focused light source (λ = 550 nm) illuminates the sampling volume. When a particle traverses this volume, it generates forward-scattered light, which is magnified by the microscope and recorded as an image on the CMOS sensor. The microscope features a magnification (*M*) of 2.5×, and a numerical aperture (*NA*) of 0.08, while the CMOS sensor comprises 1248 × 1048 pixels with a pixel size of 4.0 μm and a frame rate of 200 Hz. To minimize motion-induced image blur, the LED exposure time is set to 1 μs. Based on these optical specifications, the theoretical detection range of the LCPIS is 4-300 μm. The lower detection limit (4 μm) is governed by the diffraction limit (approximately 4.2 μm) in accordance with the sampling theorem. The upper detection limit of 300 μm is primarily determined by the effective field-of-view (*FOV*) of the CMOS sensor and the dimensions of the image processing window. This limit has been verified through comparison with ground-based measurements of ice crystals (Cai et al., 2024). This range encompasses the characteristic size distributions of sea fog and low-level clouds.

Observational data are transmitted wirelessly with a 10 MHz bandwidth across a frequency band of 403 MHz (vertically polarized). To amplify the radio frequency (*RF*) signals, a power amplifier module centered at 400 MHz (with a ±15 MHz passband) is employed, delivering a maximum output power of 1 W (+30 dBm). The ground station utilizes a directional Yagi antenna mounted on a rotating gimbal for autonomous tracking (Fig. 2e). This configuration ensures signal stability and robust data acquisition, enabling real-time monitoring of LCPIS measurements as the probe traverses cloud and fog layers. Such near-instantaneous feedback is critical for accurately identifying the timing of cloud-base penetration and ensuring high-fidelity data collection during the stratus-to-fog transition.

2.2.2 Calibration of LCPIS sampling volume

The sampling volume directly governs the accuracy of particle number concentration retrievals. Therefore, its precise determination is crucial. Due to diffraction and the finite depth of focus inherent in optical imaging, particles displaced from the focal plane exhibit defocusing. The magnitude of this defocus is a function of both the axial displacement from the focal plane and the particle diameter (*D*). Figure 3 depicts images of standard glass microspheres (9000 Series, Thermo Fisher Scientific) at various axial positions. These borosilicate or soda-lime spheres are NIST-traceable, with mean diameters and uncertainties of 5 μm (4.3 μm±0.6 μm), 10 μm (9.6 μm±0.6 μm), 20 μm (22.2 μm±0.9 μm), 30 μm (32.5 μm±1.2 μm), 50 μm (49.3 μm±1.4 μm), and 100 μm (97.7 μm±2.2 μm). Observation of Fig. 3 reveals that the optical contrast of smaller particles diminishes more rapidly than that of larger particles as axial distance increases, resulting in a narrower window of detectability. If the interval between acceptable defocus limits is defined as the sampling depth of field (*DOF*), it follows that the *DOF* is a size-dependent parameter. Consequently, applying a uniform *DOF* across the entire spectrum would introduce systematic biases, notably the underestimation of fine-mode particles and the overestimation of coarser particles. Thus, the key to volume calibration lies in establishing a quantitative relationship between the *DOF* and particle size.

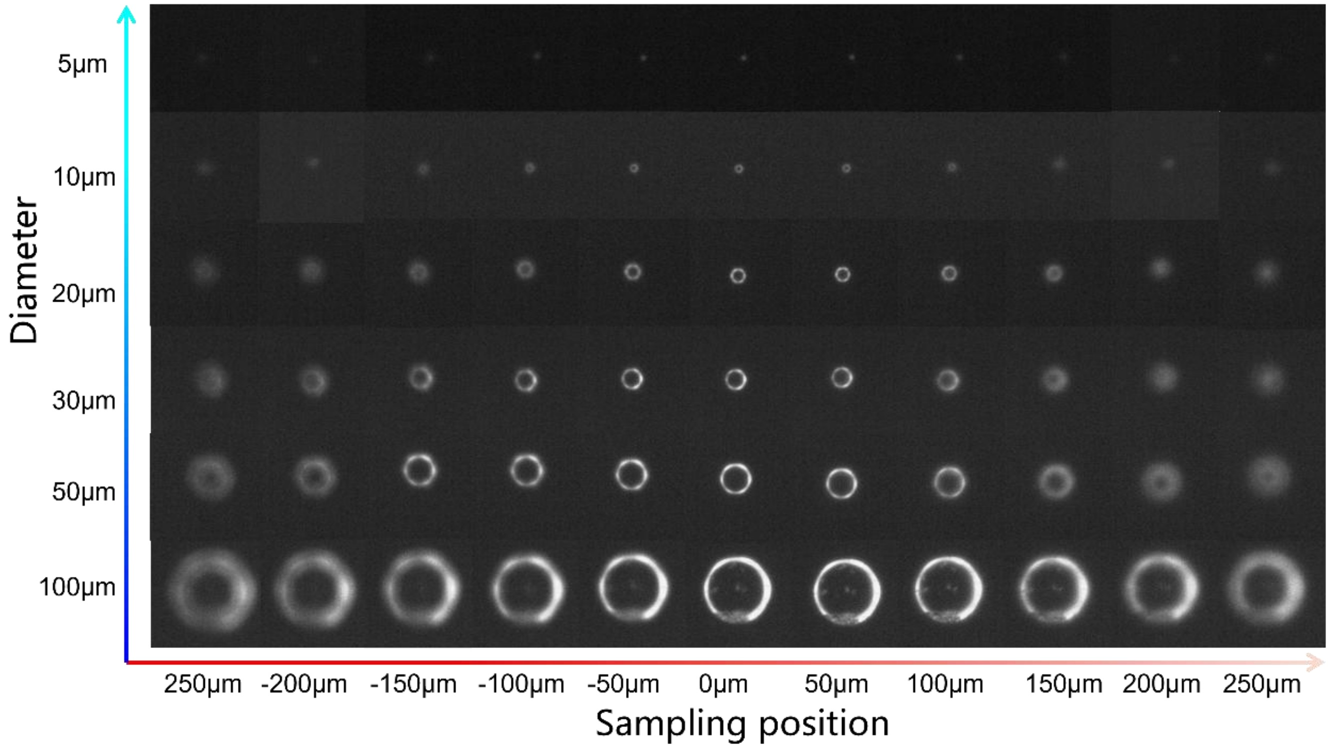

Figure 3. Shadowgraph images of NIST-traceable glass microspheres of various diameters recorded at incremental axial displacements from the focal plane (where 0 μm denotes the plane of best focus).

The calibration procedure follows the methodology described by Cai et al. (2024). Standard particles suspended in deionized water were loaded into a 2-mm-pathlength cuvette, which was mounted on a precision translation stage (±1 μm accuracy) and scanned along the optical axis (*z*-axis) in 10 μm increments. At each *z*-position, 100-200 images were acquired to ensure statistical robustness. The effective *DOF* is defined as the Δz range within which particle images satisfy a predefined sharpness criterion (*F*):

$$F = \frac{\sum_{x,y} \left| \nabla I(x,y) \right|}{I_{\max} - I_{\min}} \tag{3}$$

where $\nabla I(x,y)$ is the gradient distribution of the particle image, and $I(x,y)$ represent the pixel gray values at position (*x*, *y*). Values of *F* approaching 1 correspond to sharp edges, while values nearing 0 indicate significant blurring. In this study, a threshold of $F > 0.3$ is adopted as the criterion for acceptable out-of-focus limits. This threshold was validated against NIST-traceable standards to ensure that diameter retrieval uncertainties remain below 10%. From this criterion, the size-dependent *DOF* was derived (Table 1) and fitted to the following empirical relationship:

$$y = \mathrm{a} \times D + b \tag{4}$$

where D is the particle diameter (μm), and y is the sampling *DOF* (μm). The regression yielded coefficients of $a = 4.9$ and $b = 137.5$ ($R^2 = 0.944$). The sampling volume (V) for a given particle size is then computed as $V = DOF \times A$, where A represents the effective imaging area of the CMOS sensor.

Table 1 Sampling depth of field corresponding to different particle sizes

Diameter	4.3μm	9.6μm	22.2μm	32.5μm	49.3μm	97.7μm
DOF	102μm	178μm	282μm	346μm	384μm	591μm

2.2.3 Particle size accuracy calibration

To validate the measurement accuracy of the LCPIS for cloud and fog droplets, a statistical analysis was conducted using the retrieval results of NIST-traceable standard particles. Employing the data processing workflow detailed in Sect. 2.3, standard particle images were subjected to automated detection, edge extraction, and morphological analysis to quantify instrumental measurement errors and uncertainties.

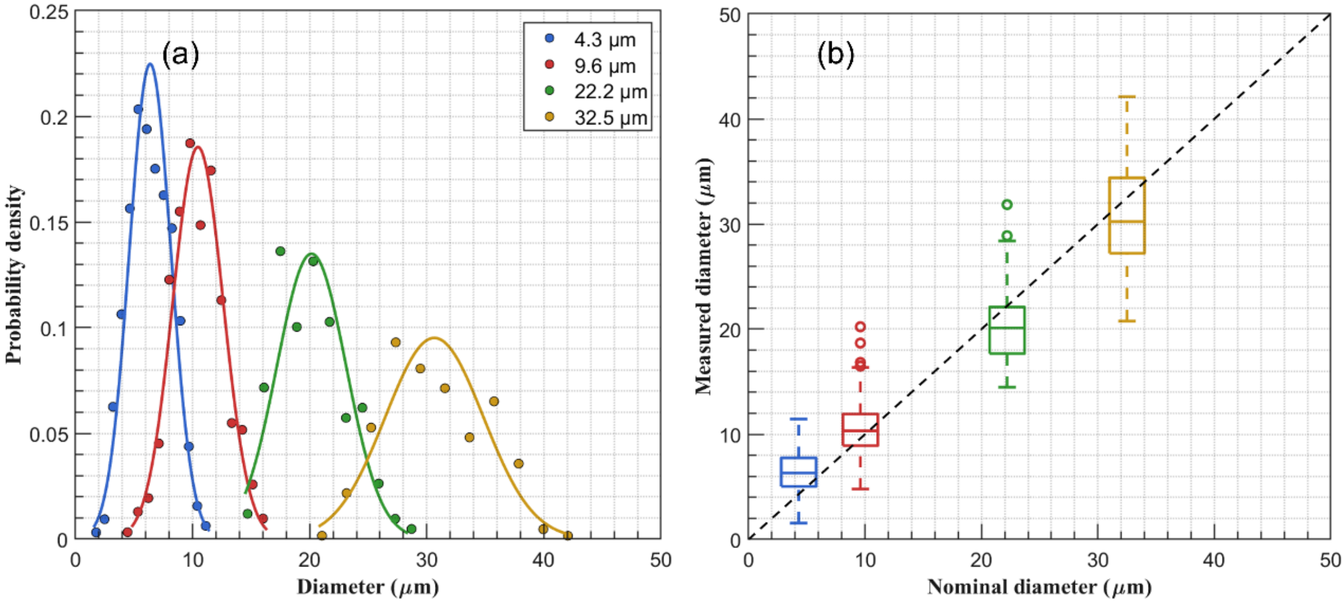

Figure 4. Calibration results of standard glass microspheres. (a) Probability density distributions (PDDs) of the measured particle sizes, (b) box plot of nominal diameter versus measured diameter.

Figure 4a illustrates the size-resolved probability density distributions (PDDs) for monodisperse microspheres across four nominal diameters (4.3, 9.6, 22.2, and 32.5 μm). For each standard specification, the modal diameters closely align with their respective nominal values, demonstrating the absence of any significant systematic bias within the optical imaging system. The sample size, mean diameter, and standard deviation for these four specifications are (444, 6.37 μm, 1.77 μm), (353, 10.56 μm, 2.31 μm), (301, 20.22 μm, 3.06 μm), and (307, 30.64 μm, 4.19 μm), respectively. Compared with the nominal values, the measurements for smaller particles (4.3 and 9.6 μm) exhibit a slight overestimation, whereas those for larger particles (22.2 and 32.5 μm) show a minor underestimation (Fig. 4b). This size-dependent behaviour is primarily attributed to diffraction-induced edge broadening for smaller spheres and depth-of-field contrast attenuation for larger ones. Nevertheless, the relative errors across all calibrated ranges remain strictly within 10%, demonstrating high measurement precision. This exceptional accuracy satisfies the rigorous requirements for cloud and fog droplet microphysical characterization, thereby providing a robust foundation for the datasets obtained during subsequent field observations.

2.3 Image processing and microphysical parameter retrieval

The CMOS sensor captures high-resolution particle images with grayscale values ranging from 0 to 255. Raw frames typically occupy ~5 MB (1248 × 1048 pixels at 8-bit depth). Due to the limited bandwidth of the wireless telemetry system, transmitting full-resolution imagery is prohibitively data-intensive. Instead, an onboard region-of-interest (*ROI*) extraction algorithm is employed to segment candidate hydrometeors prior to transmission. To ensure robustness under varying light conditions, a dynamic thresholding approach is utilized. First, a global grayscale histogram is generated to characterize the pixel intensity distribution. Using the total pixel count, a cumulative distribution function (*CDF*) is established. The pixel intensity at the 30th percentile is defined as the dark level (representing the uniform background), while the 95th percentile serves as the dynamic threshold for particle detection. Particle candidates are identified by convolving the image with a 5 × 5 pixel sliding window. The average grayscale value within each window is calculated. If the average grayscale value within a window exceeds the dynamic threshold, the corresponding pixel data and spatial coordinates are preserved for transmission.

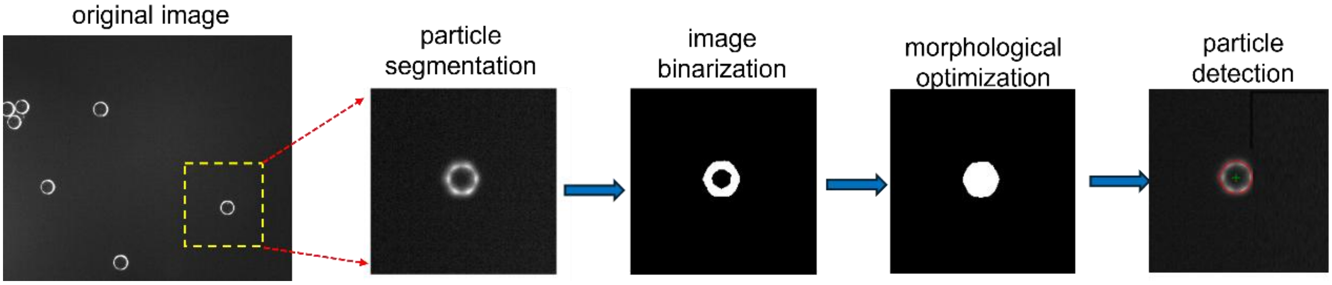

Figure 5. Schematic of the automated particle image processing algorithm, comprising stages of background subtraction, adaptive binarization, morphological filtering for noise reduction, and the final derivation of droplet microphysical parameters.

Figure 5 depicts the particle image processing workflow, encompassing image enhancement, binarization, morphological operations, and parameter extraction. Upon reception at the ground station, segmented images undergo post-processing to extract morphological and microphysical parameters. Image enhancement is first applied to suppress static background artifacts and sensor noise. Adaptive binarization is then performed using Otsu’s method, which determines the optimal threshold by maximizing inter-class variance to ensure robust segmentation of particles from the background. During morphological processing, opening operations (erosion followed by dilation) effectively eliminate salt-and-pepper noise and decouple weakly overlapping particles, while closing operations (dilation followed by erosion) fill internal voids and smooth boundary contours. Collectively, these operations preserve the morphological fidelity of the binary mask, facilitating the accurate quantification of geometric attributes such as centroid coordinates (x, y) and equivalent diameter(D).

Microphysical parameters are retrieved at a 1 s temporal resolution. Based on the quantified geometric features, the total number of particles detected within each 1 s interval is normalized by the size-dependent sampling volume to derive the instantaneous droplet number concentration (NC). Further calculations yield other key microphysical parameters, including the mean diameter (D_a) and liquid water content (LWC). These parameters are defined as follows:

$$NC_i = \frac{n(D_i)}{V(D_i)} \tag{5}$$

$$NC = \sum_{i=1}^{N} NC_i \tag{6}$$

$$D_a = \frac{1}{NC}\sum_{i=1}^{N} NC_i \times D_i \tag{7}$$

$$LWC = \frac{\pi}{6}\sum_{i=1}^{N} \frac{n(D_i) \times \rho_w \times D_i^3}{V(D_i)} \tag{8}$$

where D_i, $n(D_i)$ and $V(D_i)$ denote equivalent diameter, the particle count and the sampling volume of the i-th size bin, respectively; ρ_w is the density of liquid water. and N represents the total number of size bins. Analogous to the data processing protocol of the FM-120 fog monitor, the LCPIS measurements were discretized into size bins. The binning resolution was set to 1 μm for the 4-13 μm diameter range and 2 μm for diameters exceeding 14 μm. This scheme ensures that the resulting droplet size distributions are compatible with standard commercial probes and facilitates direct comparison with previous studies.

3 Results of the stratus-fog-stratus evolution process

3.1 Overview of surface observations

Figure 6 presents UAV-derived imagery and ground-based photographs depicting the lifecycle of the stratus-fog-stratus transition. Specifically, Fig. 6a presents an aerial view captured during the UAV sampling flight, providing direct visual evidence of the simultaneous occurrence of sea fog over the marine environment and low-level stratus over the adjacent terrestrial surface. Complementing this, the ground-based photographs displayed in Figs. 6b-d document the evolving atmospheric states and surface visibility at 09:00 UTC on 15 May (pre-fog stratus), 18:00 UTC on 15 May (sea fog), and 07:00 UTC on 16 May (post-fog stratus), respectively, illustrating the continuous stratus-fog-stratus transition. The ground-based photograph from 09:00 UTC on 15 May (Fig. 6b) indicates that the study area was initially characterized by an extensive and continuous stratiform deck. These clouds enhanced longwave radiative cooling at the surface, leading to a rapid reduction in the near-surface dew point depression. This facilitated near-surface saturation, thereby establishing favourable conditions for subsequent stratus lowering and the onset of surface-level fog (Fig. 6c). Following the dissipation stage on 16 May (Fig. 6d), the incoming shortwave radiation was significantly enhanced compared to the pre-fog period.

Figure 6. Aerial photographs of the cloud/fog evolution: (a) stratus and sea fog coexist captured by the UAV (08:30 UTC 15 May); (b) pre-fog low stratus (09:00 UTC 15 May); (c) dense sea fog peak (18:00 UTC 15 May); (d) post-fog low stratus (07:00 UTC 16 May).

The life cycle of sea fog is intrinsically linked to synoptic-scale circulation patterns and meteorological systems. In this study, the ERA5 reanalysis dataset (horizontal resolution 0.25° × 0.25°) from the European Centre for Medium-Range Weather Forecasts (ECMWF) was employed to characterize the synoptic forcing associated with this fog event. Synoptic analysis reveals that on 15 May, the Shandong Peninsula was situated downstream of a weak 500 hPa ridge. The associated subsidence promoted the establishment and maintenance of a stable marine boundary layer (MBL) over the Yellow Sea. By 06:00 UTC on 15 May, the 850 hPa wind field had transitioned from a northerly to a southerly regime, followed by a gradual intensification. Diagnostic analyses of the vertically integrated moisture divergence (*VIMD*; see Appendix A, Figs. A1e-h) indicate a prominent moisture convergence zone that emerged along the coast as the fog matured between 10:00 UTC on 15 May and 16:00 UTC on 15 May. This persistent moisture convergence, synergistically coupled with diabatic surface cooling induced by the preceding low-level cold advection (Figs. A1a-b), established a highly stable synoptic environment conducive to advection-radiation fog formation. By synthesizing these spatio-temporal dynamics, we conclude that this sea-fog event was primarily driven by the interplay between the initial cooling of the marine boundary layer and subsequent weak, poleward warm-moist advection. Furthermore, the stratus-lowering process served as the critical trigger facilitating the downward grounding of the cloud base to intercept the surface, representing the defining characteristic of this complex cloud-fog transition.

275 Surface visibility measurements provide a comprehensive record of the macroscopic evolution of this sea fog event. As shown in Fig. 7a, a significant reduction in visibility commenced at the Huangdao station at 15:30 UTC on 15 May, with values falling below 1 km. Visibility declined sharply to a minimum of approximately 100 m around 18:20 UTC on 15 May, satisfying the World Meteorological Organization (WMO) criterion for dense fog (visibility < 500 m). Following 21:00 UTC on 15 May, visibility gradually recovered to levels exceeding 1 km, signifying the dissipation of the primary dense-fog stage.

280 Concurrently, near-surface meteorological variables exhibited characteristic dense-fog conditions: the air temperature remained stable at approximately 14 °C, consistent with the thermal conditions required for condensation; the relative humidity remained persistently above 90%, maintaining a near-saturated environment; and surface wind speeds remained light (1-2 m/s), with a predominant southeasterly component. These stagnant conditions limited the turbulent mixing of moisture, while the sustained southeasterly flow ensured a continuous supply of water vapour from the Yellow Sea. Together, 285 these factors established a local environment favorable for the maintenance of dense fog.

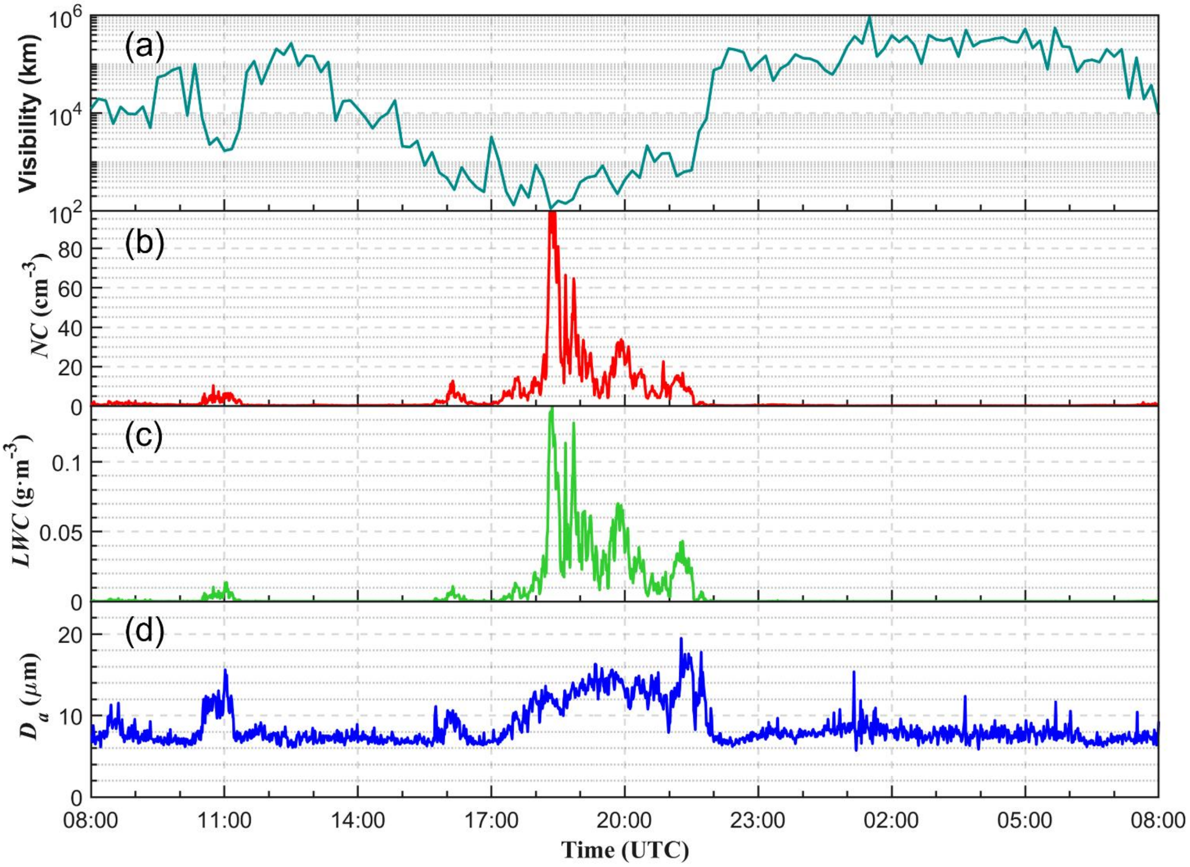

Figure 7. Time series of near-surface meteorological and microphysical parameters observed at the Huangdao site: (a) Visibility; (b) Fog droplet number concentration (*NC*); (c) liquid water content (*LWC*); (d) mean droplet diameter (*D*a).

https://doi.org/10.5194/egusphere-2026-3143
Preprint. Discussion started: 24 June 2026

Continuous observations from the ground-based lightweight cloud particle imager (Figs. 7b-d) provide further insight into the microphysical evolution of the fog event. As illustrated in Fig. 7b, during the pre-fog stage, the near-surface droplet number concentration (*NC*) was below 10 $\mathrm{cm^{-3}}$, the liquid water content (*LWC*) was negligible (≈ 0 $\mathrm{g \cdot m^{-3}}$), coinciding with visibility exceeding 10 km. During the dense-fog stage, *NC* increased to approximately 100 $\mathrm{cm^{-3}}$ at about 18:30 UTC on 15 May, coinciding with a substantial rise in *LWC*. This behaviour indicates efficient cloud condensation nuclei (CCN) activation and subsequent droplet growth via vapour diffusion. The mean droplet diameter (D_a) also gradually increased (Fig. 7d), which we attribute to the gravitational settling of larger cloud droplets from the overlying stratus layer and the inhibition of droplet evaporation within the near-saturated environment. After 21:00 UTC on 15 May, despite visibility exceeding 2 km, the instrument detected a sparse population of residual large droplets ($D_a \approx 12$ μm, $LWC = 0.03$-0.05 $\mathrm{g \cdot m^{-3}}$), potentially associated with light drizzle observed near the surface. On 16 May, enhanced shortwave heating elevated the near-surface temperature and lowered the relative humidity, triggering droplet evaporation and the subsequent thinning of the stratus layer. This resulted in a sharp decline in *NC* and *LWC*, with visibility improving to > 5 km, marking the complete dissipation of the fog event.

To characterize the fine-scale vertical structure of the MABL, nine UAV vertical profiling flights (SP01-SP09) were conducted. The specific timing of these flights is detailed in Table 2. Sampling specifically targeted the critical stratus-to-fog transition period between 08:00 UTC on 15 May and 10:30 UTC on 16 May, spanning the evolution from the pre-fog to the dissipation stages. The UAV platform, equipped with the Lightweight Cloud Particle Imager Sonde (LCPIS), featured a single-flight endurance of ~30 minutes, facilitating continuous vertical profiling of thermodynamic variables and hydrometeor microphysics within the boundary layer. Prior to the field campaign, the temperature and humidity sensors were calibrated using a standard radiosonde ground-check chamber to ensure measurement accuracy. Additionally, the imaging performance of the LCPIS was validated in situ by dispersing monodisperse calibration beads across the sampling aperture using a high-pressure gas canister and a particle generator, confirming the instrument’s capability to accurately characterize droplet size distributions.

Table 2 Summary of UAV vertical profiling flights

Profile number	weather phenomena	Number of take-offs	Date	Start time（UTC）	End time（UTC）
SP01	stratus cloud	2	2025-05-15	08:31	08:52
SP02	stratus cloud	2	2025-05-15	11:54	12:45
SP03	stratus cloud	2	2025-05-15	14:15	14:42
SP04	advection fog	2	2025-05-15	15:29	15:55
SP05	advection fog	1	2025-05-15	17:30	18:00
SP06	advection fog	2	2025-05-15	18:05	19:02
SP07	stratus cloud	1	2025-05-15	22:06	22:47
SP08	stratus cloud	1	2025-05-16	07:22	07:42
SP09	stratus cloud	2	2025-05-16	09:19	10:21

3.2 Pre-transition stratus stage

This stage constitutes the initial stage of the stratus-to-fog transition and serves as a critical period for atmospheric preconditioning regarding moisture and aerosol particles. The evolution of the thermodynamic, kinematic, and moisture structures within the marine atmospheric boundary layer (MABL) during this period significantly modulates the subsequent onset and intensification of the fog.

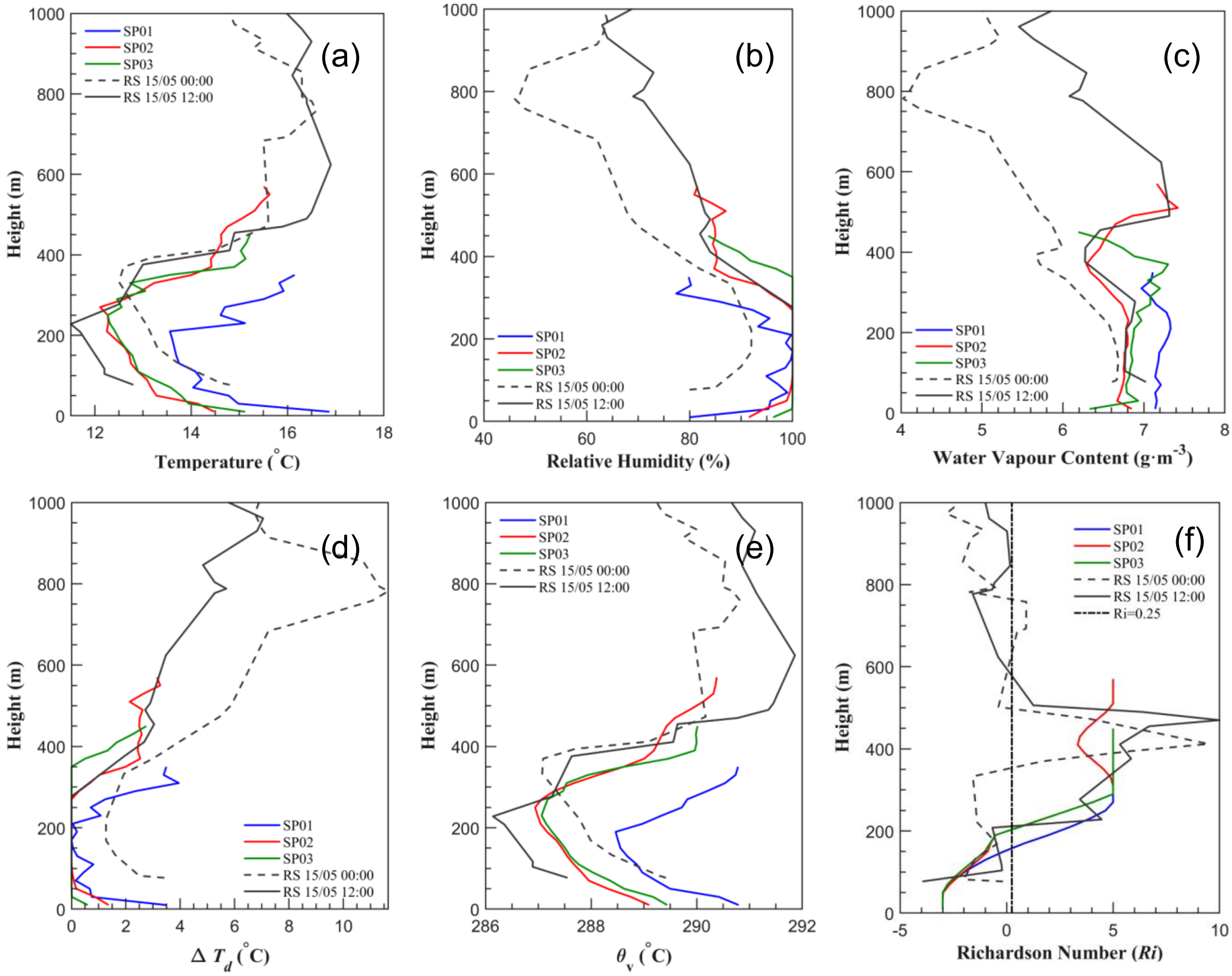

Figure 8. Vertical profiles of thermodynamic and stability parameters prior to the fog outbreak: (a) air temperature (*T*); (b) relative humidity (*RH*); (c) water vapour content (*q*); (d) dew point depression (ΔT_d); (e) virtual potential temperature (θ_v); and (f) Richardson number (*Ri*). Data points represent statistical averages calculated over 20 m altitude intervals.

Figure 8 depicts the vertical profiles of air temperature (*T*), relative humidity (*RH*), water vapour content (*q*), dew point depression (ΔT_d), virtual potential temperature θ_v, and Richardson number (*Ri*) during the three initial sampling periods

(SP01-SP03), as measured by the LCPIS system. Both the thermodynamic sensors and the cloud particle imager within the LCPIS operate at a temporal resolution of 1 s. Given a mean ascent rate of 1-2 m/s, the system achieves a native meter-scale resolution. To ensure statistical representativeness and reduce small-scale noise, the data were averaged over 20 m vertical intervals. To validate the UAV data, conventional radiosonde observations at 00:00 and 12:00 UTC on 15 May are included for comparison. The temperature profiles (Fig. 8a) reveal a pronounced inversion layer below 400 m, exhibiting marked temporal evolution. During SP01 (~08:30 UTC), the inversion base and top were situated at 210 m and 230 m, respectively, with a lapse rate of 1.56 °C·(100 m)$^{-1}$. By SP02 (11:54-12:45 UTC), the inversion base lifted to 270 m and the top reached 530 m, with the intensity increasing to 3.5 °C·(100 m)$^{-1}$. During SP03 (14:15–14:42 UTC), the base and top lowered to 250 m and 390 m, with the intensity weakening to 2.9 °C·(100 m)$^{-1}$. The RH profiles (Fig. 8b) indicate the lower MABL (100-300 m) remained near-saturated (≈ 100 %), providing a sufficient moisture reservoir for cloud droplet activation and maintenance. The temperature profiles retrieved by the LCPIS during SP02 and SP03 demonstrate strong agreement with the 12:00 UTC sounding, despite a slight positive bias of approximately 0.5 °C observed within the lowest 300 m. Above this altitude, the profiles converge and become nearly identical, thereby validating the reliability of the UAV-based measurements across the broader Marine Atmospheric Boundary Layer (MABL). Figure 8c shows that water vapour content remained above 7 g·m^{-3} within the lowest 400 m throughout the pre-fog period, with a weak vertical gradient. This vertically uniform moisture distribution, together with the near-saturation conditions ($RH \approx 100\%$), indicates that the sub-inversion layer was well-supplied with moisture, primarily sustained by sustained southerly advection and limited vertical mixing due to the capping inversion.

To further diagnose the MABL state, this study calculated the dew point depression and virtual potential temperature, and introduced the Richardson number (*Ri*) to quantitatively evaluate dynamical stability. *Ri* is a dimensionless parameter representing the ratio of buoyancy-produced to shear-produced turbulent kinetic energy:

$$Ri = \left(g/\theta_v\right)\cdot\left(\partial\theta_v/\partial z\right)/\left[\left(\partial u/\partial z\right)^2 + \left(\partial v/\partial z\right)^2\right] \tag{9}$$

where g is the gravitational acceleration, θ_v is the virtual potential temperature, and u and v are the horizontal wind components. Sounding wind data were interpolated to the 20 m height intervals of the LCPIS utilizing the Piecewise Cubic Hermite Interpolating Polynomial (PCHIP) method (Rabbath and Corriveau, 2019) , ensuring consistency with the thermodynamic gradient scales. For the pre-fog and fog stages (SP01-SP06), we used the radiosonde launch at 12:00 UTC on 15 May; for the post-fog stage (SP07-SP09), we used the launch at 00:00 UTC on 16 May. A regime where $Ri < 0$ signifies an unstable layer characterized by vigorous turbulence; $0 < Ri < 0.25$ denotes a neutral to weakly stable layer dominated by shear-induced mixing; and $Ri > 0.25$ represents a stable regime in which turbulence is effectively suppressed.

The dew point depression profiles (Fig. 8d) show values near 0 °C below 300 m, indicating saturation. Notably, from SP01 to SP03, the altitude at which the dew point depression reached 0 ℃ ascended significantly from the near-surface, indicating the progressive accumulation of water vapour under stable stratification-a precursory signal for stratus lowering and fog transition. The θ_v profiles (Fig. 8e) reveal finer thermodynamic evolution: θ_v was higher during the day (SP01) and significantly lower at night (SP02, SP03), reflecting the diurnal cycle. The transition point where θ_v begins to increase with height aligns precisely with the inversion base, indicating a stable layer shaped by surface radiative cooling. The *Ri* profiles (Fig. 8f) reveal a critical kinematic structure: below ~200 m, *Ri* was generally negative, suggesting a well-mixed layer driven by weak wind shear or residual turbulence. Above 200 m, *Ri* increased rapidly beyond the 0.25 threshold, forming a deep, dynamically stable layer. This "bottom-mixed, top-stable" vertical configuration functions as a "thermodynamic-kinematic capping inversion" that effectively inhibits the upward diffusion of water vapour and facilitates its near-surface accumulation for the subsequent rapid fog development.

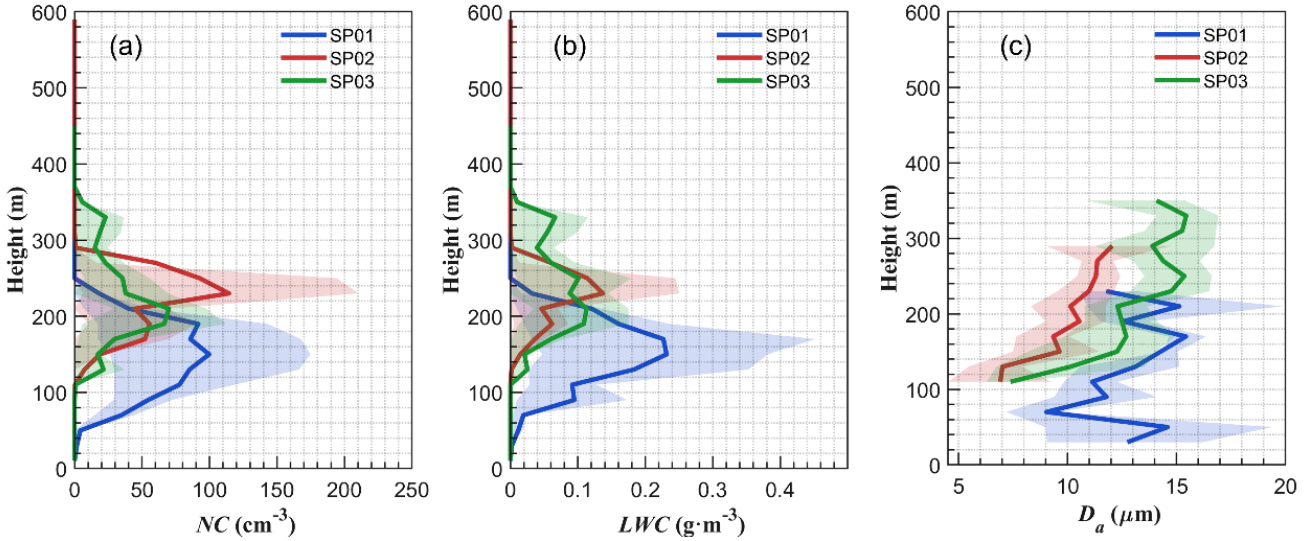

Figure 9. Vertical profiles of droplet microphysical parameters prior to the sea-fog onset: (a) droplet number concentration (NC); (b) liquid water content (LWC); and (c) arithmetic mean droplet diameter (Da). Data points represent statistical averages calculated over 20 m altitude intervals. The shaded envelopes denote the interquartile range (25th to 75th percentiles).

Figure 9 presents microphysical profiles during the pre-fog stages. Significant gradients in *NC* and *LWC* were observed within the weak mixing layer below 300 m (Figs. 9a, b). In SP01, the *NC* peak occurred between 160-180 m proximal to the inversion base, suggesting droplet accumulation induced by the capping effect of the stable stratification. In SP02 and SP03, the *NC* peak altitudes lifted to 240 m and 200 m, respectively, following the shift of the inversion base. Notably, by SP03, *NC* attained the greatest vertical homogeneity among the three periods, reflecting the thickening of the saturated layer facilitated by weak turbulent mixing. Regarding the mean diameter (D_a, Fig. 9c), the largest values (10-15 μm) were found in SP01, while SP02 showed the smallest and SP03 intermediate values. This suggests that daytime droplets grew larger through collision-coalescence, whereas nocturnal activation increased the number concentration of smaller droplets. Immediately prior to fog formation (SP03), droplets within the mixing layer underwent further activation and attained a more uniform size distribution, accompanied by a slight recovery in D_a. In summary, the thermodynamic–microphysical coupling during the pre-fog stratus stage is characterized by the capping inversion base facilitating droplet accumulation, while the

https://doi.org/10.5194/egusphere-2026-3143
Preprint. Discussion started: 24 June 2026

weak mixing layer enhances droplet activation. The expansion of the saturated layer (where dew point depression 0 °C) constitutes the primary precursory signal for the transition from stratus to sea fog.

3.3 Transition to sea fog stage

The sea fog stage, spanning periods SP04-SP06, encompasses the formation, intensification, and mature (peak intensity) stages of the fog lifecycle. Surface visibility began to decrease at 15:30 UTC on 15 May, reaching a minimum of approximately 100 m by 18:20 UTC on 15 May. During this period, the fog layer formed a vertically continuous, surface-based column, as evidenced by a significant increase in radar reflectivity and a homogeneous stratified structure (Appendix C). This peak intensity coincided with the maximum spatial extent of the positive brightness temperature difference (*BTD*) signatures observed via FY-4B satellite imagery (Appendix B).

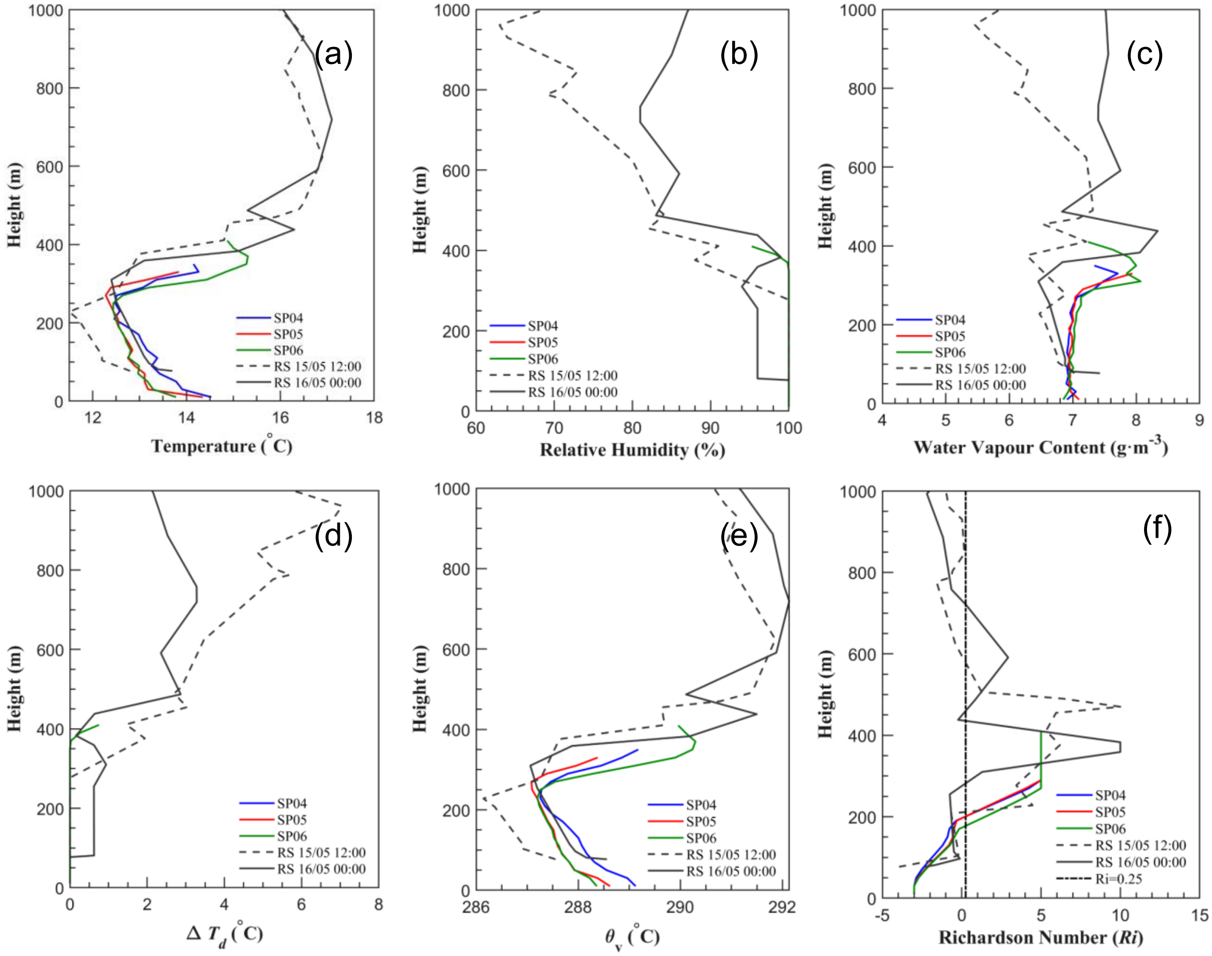

Figure 10. Vertical profiles of thermodynamic and stability parameters prior to the fog outbreak: (a) air temperature (*T*); (b) relative humidity (*RH*); (c) water vapour content (*q*); (d) dew point depression (ΔT_d); (e) virtual potential temperature (θ_v); and (f) Richardson number (*Ri*). Data points represent statistical averages calculated over 20 m altitude intervals.

Figure 10 depicts the thermodynamic and kinematic profiles during this stage. The temperature profiles (Fig. 10a) indicate that throughout the intensification stage (SP04-SP06), the inversion base persisted at a stable altitude of about 270 m. Although the UAV's operational ceiling precluded direct observation of the inversion top, sounding data from 20:00 UTC on 15 May indicated that the inversion top was located near 500 m, with the inversion intensity strengthening to approximately 5.0 °C $(100\ \mathrm{m})^{-1}$, a marked increase compared to daytime values. This pronounced, deep-seated inversion established a highly stable thermodynamic regime, effectively inhibiting vertical mixing and the upward diffusion of moisture. The *RH* profiles (Fig. 10b) demonstrate that near-saturation ($RH \approx 100\%$) extended below 400 m, reflecting a significant expansion of the saturated layer as the fog layer matured vertically. Water vapour content (Fig. 10c) was maintained at approximately 7 $\mathrm{g \cdot m^{-3}}$ throughout the lowest 300 m, exhibiting a nearly uniform vertical profile-indicating efficient turbulent mixing of moisture within the fog layer, rather than a strong advective gradient. The elevated moisture content within the fog layer also favours droplet condensation and growth, consistent with the observed increase in *LWC* and *NC* at ~200 m. Compared to the pre-fog stage, the saturated layer (dew point depression $\Delta T_\mathrm{d} \approx 0$ °C, Fig. 10d) extended to the surface, marking the complete formation of sea fog. In SP06, a sharp increase in dew point depression ΔT_d near the inversion top signified the presence of a "dry cap" which serves to suppress entrainment and moisture loss at the fog summit. The virtual potential temperature profiles (θ_v, Fig. 9e) were highly consistent across SP04-SP06, reflecting a stable thermodynamic structure. Notably, the vertical gradient of θ_v ($\partial\theta_v / \partial z \approx 0$) within the fog layer was reduced relative to the pre-fog stage, suggesting enhanced turbulent mixing and homogenization.

The Richardson number (*Ri*) profiles (Fig. 10f) delineate the critical kinematic structure sustaining the fog. Within the fog body (below the 280 m inversion base), *Ri* was generally negative, identifying a dynamically unstable region facilitating turbulent mixing. This instability is likely attributable to top-down convection induced by cloud-top radiative cooling. Such mixing contributes significantly to droplet collision-coalescence, vertical moisture redistribution, and fog homogenization. Near the inversion top, *Ri* transitioned rapidly to positive values and increased sharply with height, forming a robust dynamically stable layer. This "internally mixed, capped-stable" *Ri* profile aligns closely with the top-down mixing mechanism driven by cloud-top cooling as described by Singh et al. (2024). Although cloud-top radiation was not measured directly, the presence of the negative *Ri* zone and the downward expansion of the saturated layer provide indirect evidence of this process. This structure, acting in concert with the "dry cap" effectively traps moisture and droplets within the boundary layer, playing a decisive role in maintaining the intensity and persistence of the dense fog.

https://doi.org/10.5194/egusphere-2026-3143
Preprint. Discussion started: 24 June 2026

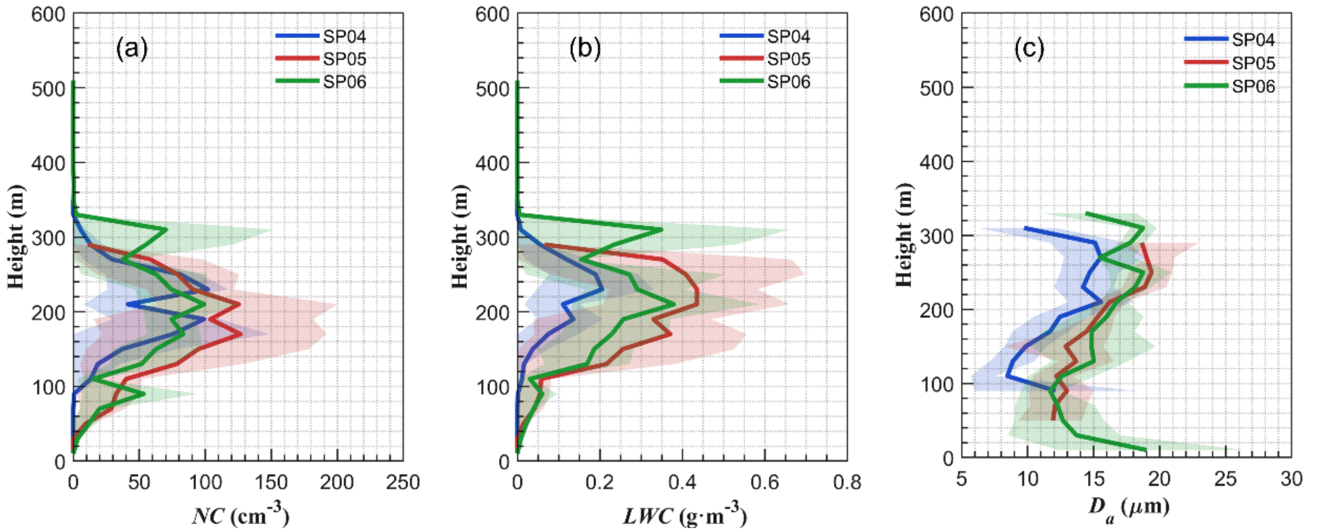

Figure 11. Vertical profiles of LCPIS microphysical parameters during the mature sea-fog stage: (a) droplet number concentration (NC); (b) liquid water content (LWC); and (c) arithmetic mean droplet diameter (Da). Data points represent statistical averages calculated over 20 m altitude intervals. The shaded envelopes denote the interquartile range (25th to 75th percentiles).

Figure 11 presents the microphysical profiles during the fog event. The profiles of *NC* and *LWC* across the three periods show similar morphologies, with values increasing and then decreasing with height. The maxima occurred near 200 m, coinciding spatially with the negative *Ri* mixing zone. Period SP05 featured the highest peak *NC* (~ 120 cm^{-3}) and *LWC* (~ 0.45 g·m^{-3}), corresponding to the stage of minimum visibility. This suggests that the vigorous mixing layer facilitated aerosol activation and droplet growth. The mean diameter (D_a) ranged from 6~20 μm (Fig. 11c) with a uniform vertical distribution, reflecting the homogenizing effect of turbulent mixing. Compared to the pre-fog stage, the peak altitudes of *NC* and *LWC* exhibited greater vertical consistency, and profile morphologies were more robust. This indicates that the capping inversion and the positive *Ri* layer effectively sequestered microphysical processes within the boundary layer. In summary, the thermodynamic–microphysical coupling during the sea fog intensification stage is governed by a tripartite mechanism: the intense inversion provides a stable thermodynamic background; the negative *Ri* zone drives turbulent mixing that promotes droplet activation and homogenization; and the positive *Ri* zone, combined with the "dry cap" forms a sealed upper boundary. Together, they create an efficient "capture system" for water vapour and droplets, supporting the sustained development of dense sea fog.

3.4 Re-lifting to low cloud stage

This dissipation stage, spanning periods SP07-SP09, marks the terminal stage of the sea fog lifecycle. It is characterized by the gradual erosion of near-surface fog as the layer lifted and transitioned back into an elevated stratus deck. Primarily driven by intensified solar shortwave radiation, this transition represents a characteristic insolation-induced dissipation mechanism.

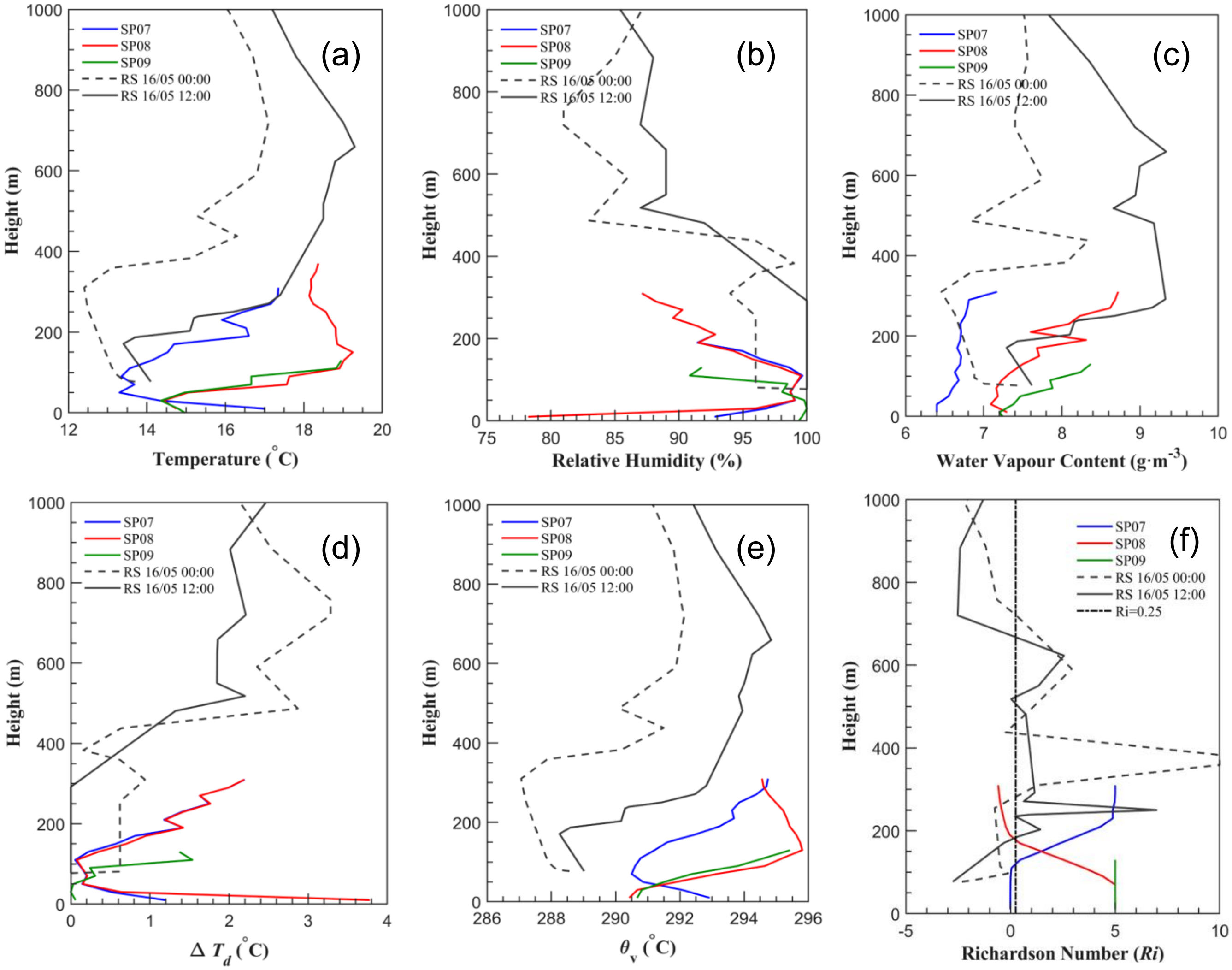

Figure 12. Vertical profiles of thermodynamic and stability parameters prior to the fog outbreak: (a) air temperature (*T*); (b) relative humidity (*RH*); (c) water vapour content (*q*); (d) dew point depression (ΔT_d); (e) virtual potential temperature (θ_v); and (f) Richardson number (*Ri*). Data points represent statistical averages calculated over 20 m altitude intervals.

Figure 12 depicts the vertical profiles of thermodynamic and kinematic parameters during the dissipation stage. As solar irradiance intensified, the boundary layer structure underwent a fundamental regime shift. Relative to the fog-maintenance stage, near-surface temperatures rose significantly (Fig. 12a), precipitating a sharp decline in relative humidity (Fig. 12b). This thermal reversal decoupled the near-surface saturation regime. The subsequent increase in saturation vapour pressure facilitated droplet evaporation, which served as the primary microphysical driver of fog dissipation. Correspondingly, the water vapour content profiles (Fig. 12c) show an increase in the lower atmosphere as evaporation released moisture, providing a local source for subsequent stratus formation. The dew point depression profiles (Fig. 12d) further elucidate the vertical redistribution of moisture. During the diurnal stage (SP07, SP08), near-surface dew point depression increased markedly, with a minimum situated at ~ 100 m, indicating the ascent of the fog top to form a nascent cloud base. During the final sampling period (SP09; 09:19-10:21 UTC), the dew point depression (T-T_d) exhibited a monotonic increase with height, reflecting the presence of dry air aloft while moisture remained sequestered near the surface. The virtual potential temperature profiles (θ_v, Fig. 12e) illustrate the reorganization of the thermodynamic structure. In SP07, θ_v initially increased and then decreased with height, with an inflection point near 100 m above which a weakly stable layer ($\partial\theta_v / \partial z > 0$) was re-established. In SP08 and SP09, θ_v increased rapidly with height, indicating the decay of the daytime convective boundary layer and the subsequent re-establishment of stable stratification extending from the surface upward. These changes mark the successful detachment of the moisture layer from the surface fog system, which persisted as a stable elevated layer. The gradient Richardson number (*Ri*) profiles (Fig. 12f) captured a fundamental shift in dynamical stability. In contrast to "sandwich" structure observed during the fog-maintenance stage (negative *Ri* internally, positive *Ri* at the top; Fig. 8f and Fig. 10f), vertical profiles of *Ri* in post-dissipation were predominantly near-zero or positive. This indicates that the boundary layer regained overall dynamical stability, which suppressed intense vertical turbulent exchange and allowed evaporated moisture and residual droplets to lift in a steady, organized manner, facilitating their reorganization into stratiform low clouds.

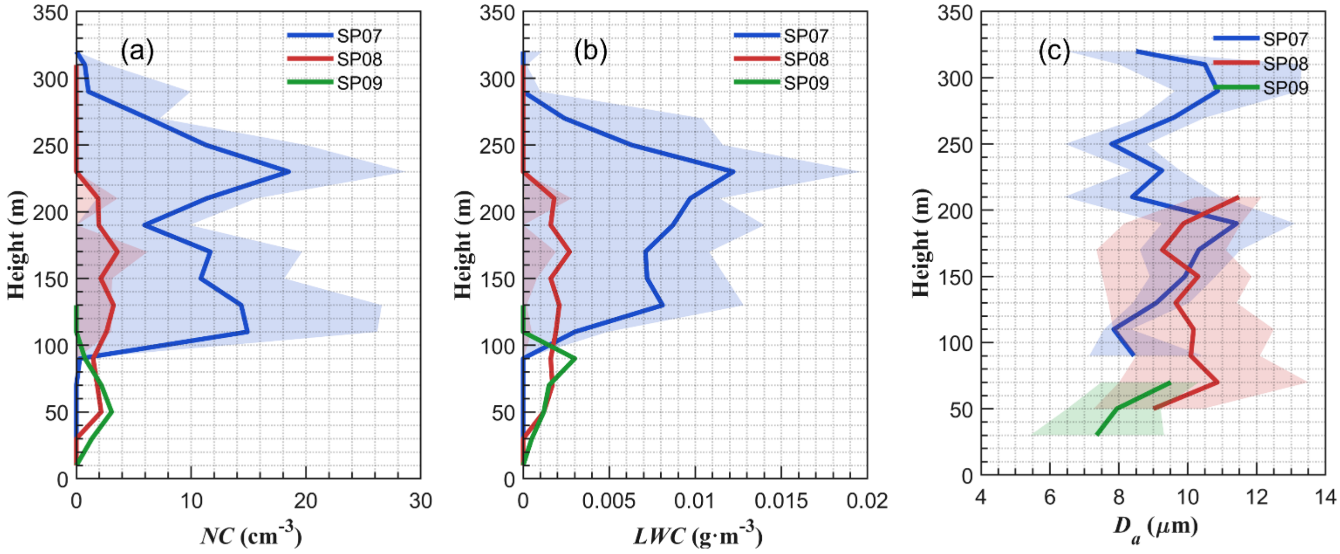

Figure 13. Vertical profiles of LCPIS microphysical parameters after the fog dissipation: (a) droplet number concentration (NC); (b) liquid water content (LWC); and (c) arithmetic mean droplet diameter (Da). Data points represent statistical averages calculated over 20 m altitude intervals. The shaded envelopes denote the interquartile range (25th to 75th percentiles).

Figure 13 presents the microphysical profiles following fog dissipation, with the timing of SP07 (22:06-22:47 UTC) coincided with the onset of solar radiation at dawn (16 May). During this initial stage, a tenuous cloud layer was observed between 100 and 300 m (Fig. 13a). These cloud altitudes correspond to the levels of minimum dew point depression (Fig. 13d) and the inflection point of θ_v (Fig. 13e). This suggests that during fog dissipation, water vapor from evaporation and residual hydrometeors ascended within the stably stratified layer and re-condensed at specific altitudes to form a stratus cloud layer. Under conditions of intense solar irradiance on 16 May, the lower atmosphere during SP08 and SP09 was primarily characterized by fractostratus, with cloud droplet number concentration (*NC*) and liquid water content (*LWC*) exhibiting significant reductions (Figs. 13a, b). Across the three periods, the mean diameter (D_a) was approximately 6~13 μm below 300 m (Fig. 13c). In summary, the thermodynamic-microphysical coupling during the re-lifting stage is defined by an insolation-driven thermal reversal (with $Ri > 0$) that suppresses turbulent mixing, allowing water vapor and residual droplets to ascend and re-condense at altitudes of 100-300 m, completing the closed-loop evolution from sea fog back to stratus.

4 Discussion

4.1 Stratus-to-fog transition mechanism and conceptual model

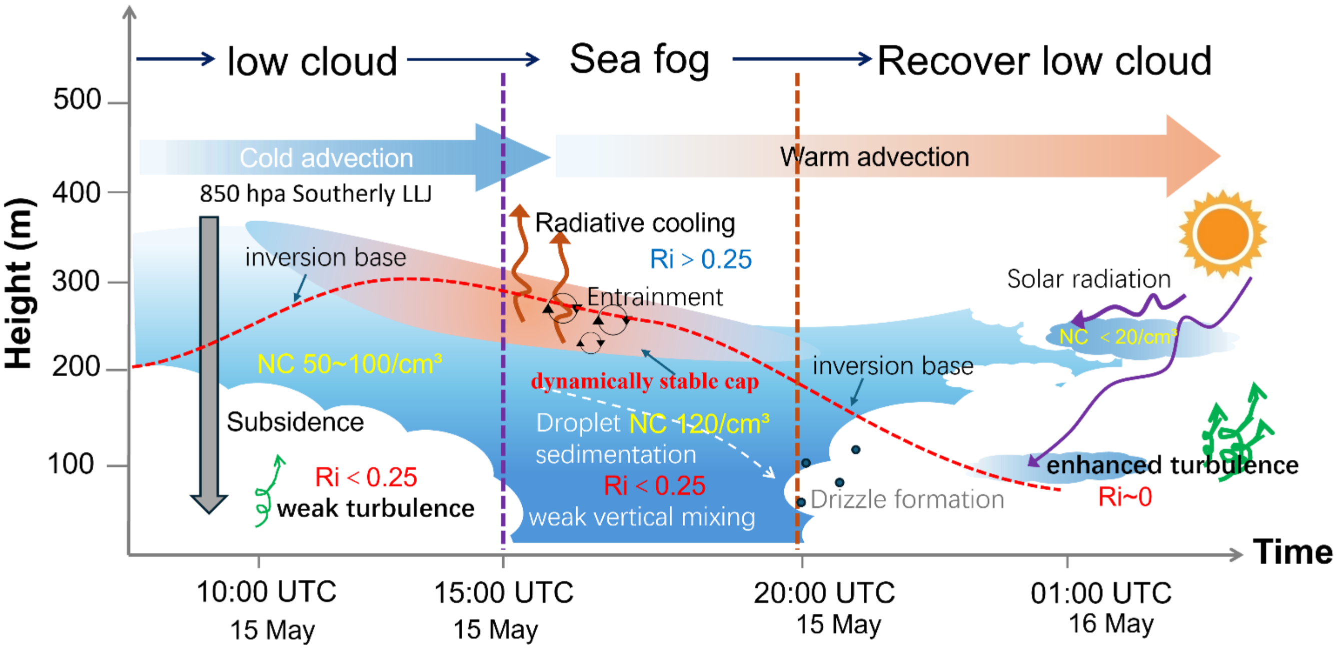

Figure 14. Conceptual model of the spatiotemporal evolution governing the advection-driven stratus-fog-stratus (SFS) transition, depicted in a time-height coordinate system. The schematic illustrates the coupled thermodynamic, radiative, and microphysical feedbacks that mediate the formation, maturation, and subsequent lifting of the cloud-fog layer.

The stratus-fog-stratus (SFS) transition along the Yellow Sea coast is governed by the synergistic interaction of synoptic-scale forcing, boundary-layer stratification modifications, and microphysical processes. Based on the preceding results, two coupled processes can be identified as governing this transition. First, top-down turbulent mixing is driven by cloud-top radiative cooling, as evidenced by the negative *Ri* within the fog layer (Fig. 10f). Second, the interplay between near-surface warm-moist advection (from the southerly regime) and pre-existing cold advection (Figs. A1a-d) establishes the thermal and moisture preconditioning. Synthesizing these observations, we propose a "three-stage, three-level" conceptual model for the SFS transition (Fig. 14). The model uses time and height as two-dimensional coordinates to characterize the spatiotemporal coupling among weather forcing, stratification adjustment, and microphysics. In the schematic, the blue region represents the saturated zone (dew point depression ≈ 0 °C), the upper red region indicates the dry cap, and the red dashed line tracks the evolution of the inversion base height.

(1) Pre-transition stratus stage: thermodynamic-dynamic preconditions

During stage 1, large-scale subsidence at 500 hPa and southerly winds at 850 hPa establish the dynamical background necessary for the formation and maintenance of the inversion layer. A shallow layer with negative *Ri* (i.e., $Ri < 0$) below the inversion base, reflecting weak wind shear and residual turbulence, whereas $Ri > 0.25$ above the inversion forms a "thermodynamic-dynamic capping inversion". This configuration promotes moisture accumulation in the near-surface layer while inhibiting upward transport, thereby creating a moisture reservoir that favours subsequent rapid fog development. Although such structures are seldom explicitly quantified in classical advection fog models, this study empirically confirms their existence through high-resolution vertical profiles.

(2) Transition to sea fog: shear-turbulence-microphysics coupling

The core of stage 2 is the positive feedback triggered by radiative cooling at the fog top. As the stratus base descends toward the surface, intensified longwave cooling at the stratus top generates buoyancy-driven turbulence ($Ri < 0$) , which transports moisture downward. The negative Richardson number (*Ri*) zone inside the fog layer (Fig. 10f) indicates active turbulent mixing, which aligns with the gravitational-settling-driven downward moisture flux proposed by Pope and Igel (2025). Simultaneously, the sedimentation and evaporation of droplets beneath the cloud further cool and moisten the near-surface layer. This process aligns with the mechanism reported by Singh et al. (2024) in Newfoundland, although the inversion layer in the Yellow Sea event was deeper (500 m vs. 300 m). Our measured droplet sizes (10-20 μm) were larger than their reported range of 10-15 μm. The former difference is likely attributable to stronger stratification associated with large-scale subsidence over the Yellow Sea, whereas the latter reflects the prevalence of sea-salt-influenced particles in this region, which promote larger droplet growth compared to the more terrestrial-aerosol-impacted environment of the North Atlantic (Pope and Igel, 2025). This comparison highlights the regional specificity of sea fog microphysics. Evidence from the numerical simulations by Pope and Igel (2025) supports this interpretation. They showed that enhanced gravitational settling under low aerosol concentrations promotes earlier fog formation and longer duration but limits fog water content via increased surface deposition. Our observations are consistent with this dual effect: the negative *Ri* zone in stage 2 (Fig. 10f) facilitates droplet sedimentation, while the dynamic stable cap ($Ri > 0.25$) suppresses entrainment. The mean droplet diameter (10-20 μm) observed during our sea fog stage suggests a regime characterized by lower aerosol loading or sea-salt dominance, consistent with the broader-distribution scenarios in their model. Finally, the ground-based number concentration (*NC*) peak (≈ 100 $\mathrm{cm^{-3}}$) showed strong agreement with the UAV-measured peak (100-120 $\mathrm{cm^{-3}}$) within the fog layer, suggesting efficient vertical mixing and confirming vertical homogeneity in droplet concentration between the surface and the core of the fog layer.

(3) Re-lifting to low cloud: Dissipation drivers (heating and shear weakening)

Stage 3 is driven by solar radiative heating. Surface warming disrupts near-surface saturation, causing *Ri* to turn almost positive and suppressing vertical turbulent exchange. Consequently, while vigorous vertical mixing is suppressed, the residual moisture and evaporated vapor ascend slowly within a stable stratification, re-condensing into low-level stratus at altitudes of 100-300 m. This mechanism explains why the fog layer does not simply dissipate in situ but instead "lifts" to transform into a stratus layer. Current numerical models often struggle to accurately simulate sea fog due to imprecise parameterizations of radiation-turbulence coupling at the inversion top and near-surface moisture accumulation. The "bottom-mixed, top-stable" structure and the quantitative evolution of *Ri* identified in this study provide diagnostic indicators for model improvement. For instance, a "stratus lowering" warning could be triggered when $Ri < 0$ is predicted below the inversion base while $Ri > 0.25$ persists above it.

Furthermore, the stabilization of *NC* at its upper bound (100-120 $\mathrm{cm^{-3}}$), concurrent with a doubling of *LWC*, could serve as a combined microphysical indicator for cloud-to-fog transitions. Future research should employ large-eddy simulations (LES) and radiative transfer models to quantify the critical conditions governing the radiation–turbulence coupling at the fog top.

4.2 Regional comparison of stratus-lowering mechanisms

The observed stratus–fog–stratus transition over the Yellow Sea exhibits distinct features compared to three previously documented fog regimes. Off the California coast, stratus lowering is primarily governed by cloud-top radiative cooling and large-scale subsidence (Koračin et al., 2001; Lewis et al., 2004), but the vertical structure of the Richardson number has not been explicitly quantified. In the Grand Banks of Newfoundland, top-down convection and droplet sedimentation dominate, with a shallower inversion (~300 m) and smaller droplets (10-15 μm) (Singh et al., 2024). Along the Atlantic coast of Western Europe, cold-moist advection combined with nocturnal cooling is the main driver (Gultepe et al., 2007). By contrast, the Yellow Sea event is characterized by: (i) a deeper inversion layer (~500 m) , likely due to stronger large-scale subsidence; (ii) a quantified Richardson number structure, with $Ri < 0$ inside the fog layer (indicating vigorous mixing) and $Ri > 0.25$ above (indicating a dynamically stable cap); (iii) larger mean droplet diameters (10-20 μm), attributed to sea-salt-dominant aerosol; and (iv) a nearly uniform vertical distribution of water vapour content (~7 $\mathrm{g \cdot m^{-3}}$) within the fog layer, indicating efficient vertical mixing of moisture rather than a persistent advective gradient. These discrepancies highlight the regional specificity of sea fog microphysics and dynamics, underscoring the need for region-specific parameterizations in numerical models.

4.3 Validation of the LCPIS and further improvements

The integration of the Lightweight Cloud Particle Imager Sonde (LCPIS) with UAV platforms significantly enhances the in situ characterization of fine-scale MABL structures. This approach mitigates the spatial and temporal limitations inherent in traditional observational platforms. Within the constraints of permissible airspace, the LCPIS enables the rapid detection of cloud and fog boundaries, facilitating high-resolution characterization of the cloud volume and the upper entrainment zone. The agile maneuverability of the UAV platform facilitates both long-range horizontal transects and high-frequency vertical profiling. Preliminary laboratory cold-chamber evaluations confirm LCPIS functionality under supercooled conditions, demonstrating its potential for imaging ice-stage hydrometeors during low-temperature missions. During field campaigns on 16 May, the LCPIS maintained robust operational performance despite ambient wind speeds at altitude reaching 14 $m \cdot s^{-1}$ and necessitating UAV wind alerts. Compared to manned aircraft or tethered balloon systems, the UAV-LCPIS architecture requires minimal logistical preparation, with full deployment achievable by two operators within approximately 30 minutes.

The LCPIS system provides concurrent measurements of thermodynamic parameters (temperature, humidity, and pressure) and hydrometeor microphysics within the boundary layer. While thermodynamic profiles can be cross-validated against standard radiosonde data, the relatively coarse vertical resolution of the latter (> 50 m) constrains direct high-resolution comparisons. More rigorous validation is feasible using high-altitude meteorological towers (> 300 m). Future efforts should prioritize the minimization of sensor hysteresis to enhance measurement fidelity. The tunable diode laser absorption spectroscopy (TDLAS) water vapour module provides critical complementary measurements, resolving moisture content within and above the cloud layer-regions where conventional capacitive *RH* sensors often suffer from saturation or hysteresis (notwithstanding consistent in-cloud readings of ~ 100% *RH*). Furthermore, integration with remote sensing platforms (e.g., cloud radar, lidar, and satellites) provides the necessary macroscopic context; here, the LCPIS serves as a high-fidelity ground-truth benchmark for refining and validating remote sensing retrieval algorithms.

A primary constraint of the current LCPIS configuration is the absence of onboard wind velocity measurements, which are essential for the closure of boundary-layer energy and moisture budgets. The integration of miniature, UAV-mounted anemometers is currently underway to address this limitation. Nevertheless, a related caveat concerns the calculation of the Richardson number (*Ri*). Because the LCPIS payload does not include an onboard anemometer, we derived vertical wind shear from radiosonde wind profiles interpolated to the UAV altitude grid. Specifically, we used the 12:00 UTC sounding on 15 May for the pre-fog and fog stages, and the 00:00 UTC sounding on 16 May for the post-fog stage. While this approach captures the large-scale shear and stability structure, it cannot resolve short-term variability or small-scale wind features within the fog layer, which may affect the instantaneous *Ri* values. Nevertheless, the sign of *Ri* (negative within the fog layer, positive above) is robust and provides meaningful dynamical insight. Future deployments of the LCPIS should incorporate a miniature wind sensor to enable fully independent *Ri* calculations. Furthermore, the LCPIS exhibits reduced sensitivity to small droplets. As described in Sect. 2.2.2, the sampling depth of field (*DOF*) for small particles (e.g., 5.3 μm) is only 102 μm, much smaller than that for larger particles (384 μm at 49. 3 μm). Consequently, small particles may be under-sampled due to the restricted effective volume. While size-dependent *DOF* corrections maintained calibration errors within 10%, systematic underestimation of number concentration (*NC*) may persist due to low image contrast and rapid droplet size distribution (*DSD*) evolution in turbulent environments. Beyond these constraints, potential sampling biases arising from non-isokinetic aspiration and sensor hysteresis during fast vertical traverses should be considered. While the UAV platform offers operational agility, the limited total sampling volume in low-number-concentration regimes may introduce statistical uncertainty in the derived *DSD*. Moreover, although onboard algorithms mitigate ambient light interference, fluctuations in optical contrast under high-irradiance conditions at the cloud top could affect the consistency of droplet sizing. Future work will incorporate computational fluid dynamics (CFD)-optimized inlet designs and enhanced shielding to further minimize these environmental artefacts. A conceptual overview of the LCPIS platform is presented in Fig. 15.

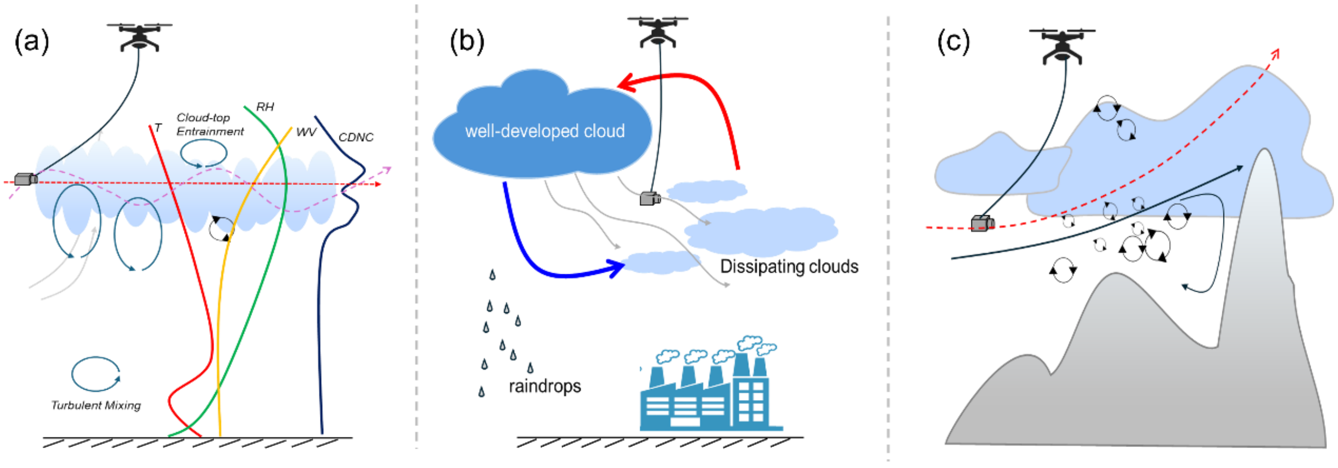

Figure 15. Conceptual overview of the UAV-borne Lightweight Cloud Particle Imager Sonde (LCPIS) platform, illustrating its high-resolution in situ observational capabilities and broad scientific applications for vertical profiling of the microphysical, thermodynamic, and dynamical structures of boundary-layer clouds and fog.

Future research aims to extend UAV–LCPIS deployments across diverse cloud and fog regimes, focusing on:

(a) High-Resolution Microphysical Mapping: Conducting horizontal and vertical profiling at low transect speeds (~2 $m \cdot s^{-1}$) to investigate fog-top radiative cooling and cloud-top entrainment dynamics.

(b) Multi-layer Cloud Characterization: Resolving the structural disparity between precipitating and non-precipitating layers to evaluate their impacts on aerosol scavenging and pollutant dispersion.

(c) Orographic Cloud Microphysics: Circumventing the limited vertical resolution of stationary platforms by providing high-resolution vertical gradients in complex mountainous terrain.

5 Summary and Outlook

In this study, we introduced the newly developed Lightweight Cloud Particle Imager sonde (LCPIS) and demonstrated its utility for investigating sea fog and low-level stratus within the marine atmospheric boundary layer (MABL). Utilizing high-resolution UAV-borne observations conducted along the Yellow Sea coast in 15-16 May 2025, our principal findings are summarized as follows:

(1) System Capabilities

The LCPIS achieves high spatiotemporal resolution vertically profiling of temperature, humidity, water vapour content, and cloud/fog microphysical properties. The LCPIS acquires measurements at 1 Hz, enabling vertical profiling with meter-scale resolution during standard UAV operations. Its compatibility with both radiosonde balloons and UAV platforms makes it a versatile instrument for multidisciplinary boundary-layer research.

(2) Three-stage Thermodynamic-Kinematic Co-evolution

The observed sea fog event underwent a distinct three-stage evolution modulated by the synergistic coupling of thermodynamic and kinematic processes. During the pre-fog low-cloud stage, the inversion base ascended from 210 m to 270 m, with the temperature gradient strengthening from 1.56 $°C\cdot(100\,m)^{-1}$ to 3.5 $°C\cdot(100\,m)^{-1}$. The Richardson number (*Ri*) was < 0.25 below the inversion (enhanced mixing) and > 0.25 above it (indicating stable suppression), a configuration that promoted near-surface moisture accumulation. In the transition to fog stage, the saturated layer extended to the surface. The inversion intensity further intensified, reaching approximately 5.0 $°C\cdot(100\,m)^{-1}$ during the fog maturity, as derived from the 20:00 UTC sounding. Within the fog layer, *Ri* became predominantly negative-indicating buoyancy-driven turbulent mixing-before increasing abruptly to > 0.25 near the fog summit, establishing a “dynamical capping inversion”. Finally, during the re-lifting to stratus stage, solar insolation disrupted the saturation regime. *Ri* transitioned to positive values, and the vertical transport of water vapor led to the reorganization of low-level clouds. The “thermodynamic-kinematic capping” structure is identified as the primary driver for surface-level fog inception, characterizing a complete life cycle from moisture pre-conditioning through rapid intensification to stable lifting.

(3) Microphysical profiles distribution

The microphysical parameters exhibited a symmetric evolution centered on the fog stage. From the initial stratus to the sea-fog stage, the droplet number concentration (*NC*) increased from 50-100 cm^{-3} to approximately 100-120 cm^{-3}, while the liquid water content (*LWC*) rose from 0.1-0.2 to 0.2-0.45 $g\cdot m^{-3}$. The arithmetic mean diameter (D_a) stabilized between 6 μm and 20 μm throughout the event.

(4) Outlook and Future Research

Several research avenues warrant further exploration to build upon these findings. First, instrument validation through dedicated intercomparison experiments-including side-by-side evaluations with established probes such as the Cloud Droplet Probe (CDP) and high-altitude meteorological towers-is necessary to quantify the absolute accuracy of the LCPIS under diverse conditions. Second, platform expansion will involve deploying the LCPIS on sounding balloons to obtain simultaneous in-situ measurements for comparison with radiosonde and cloud radar retrievals. Third, modeling integration will utilize this dataset as a high-fidelity benchmark for large-eddy simulations (LES) and single-column models (SCM) to refine the parameterization of fog-turbulence-radiation interactions. Ultimately, the LCPIS is expected to serve as a standardized tool for exploring the complex coupled microphysical and kinematic processes governing boundary-layer clouds and fog.

Appendix A: Temperature advection and vertically integrated moisture divergence

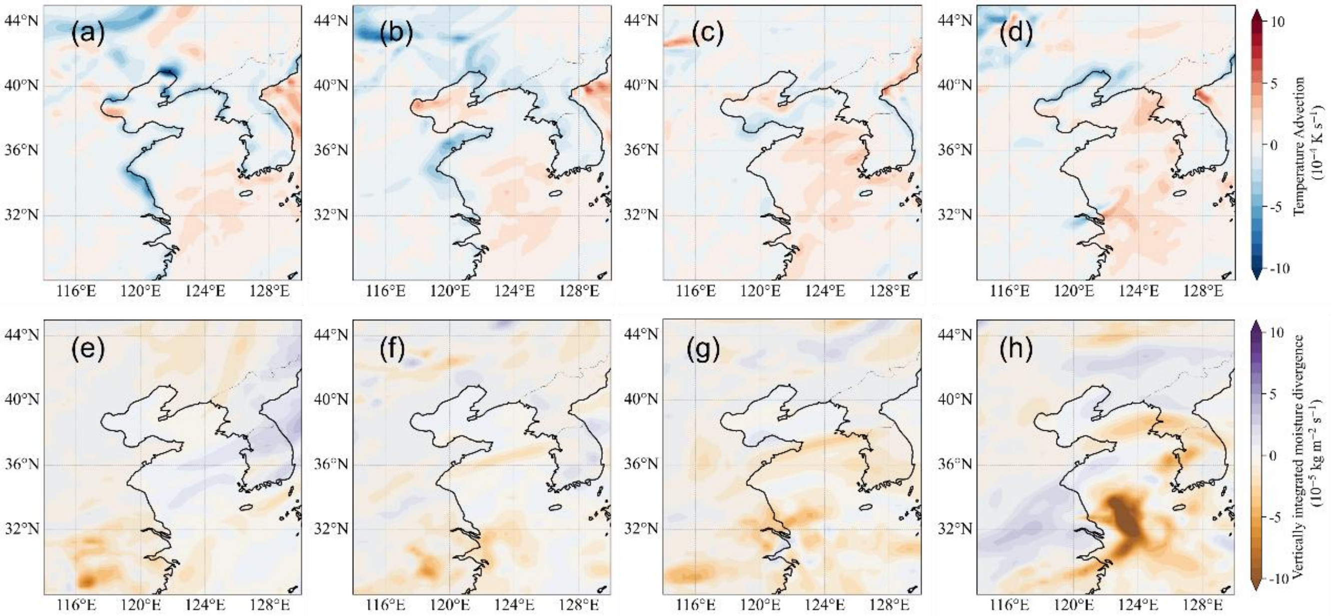

Figure A1. Horizontal temperature advection at 1000 hPa (top row) and vertically integrated moisture divergence (bottom row) over the observation area. Panels correspond to (a, e) 04:00 UTC on 15 May, (b, f) 10:00 UTC on 15 May, (c, g) 16:00 UTC on 15 May, and (d, h) 00:00 UTC on 16 May.

To investigate the thermodynamic and moisture processes driving the sea fog life cycle, horizontal temperature advection (*HTA*) and vertically integrated moisture divergence (*VIMD*) were analyzed along prevailing airflow trajectories. The parameters *HTA* and *VIMD* are defined by Eq. (A1) and Eq. (A2), respectively:

$$HTA = -\left(u\frac{\partial T}{\partial x} + v\frac{\partial T}{\partial y} \right) \tag{A1}$$

$$VIMD = \frac{1}{g}\int_{p_{top}}^{p_{surf}} \left[\frac{\partial(u \cdot q)}{\partial x} + \frac{\partial(v \cdot q)}{\partial y} \right] dp \tag{A2}$$

Where u and v denote horizontal wind components, q represents specific humidity, and g is the acceleration due to gravity. The integration is conducted from the top of the atmospheric column (p_{top}) to the surface pressure (p_{surf}). *VIMD* is a fundamental diagnostic parameter in atmospheric moisture budget analyses, as it quantifies the net horizontal flux of water vapour within the atmospheric column. Negative *VIMD* values (indicating moisture convergence) facilitate the localized

https://doi.org/10.5194/egusphere-2026-3143
Preprint. Discussion started: 24 June 2026

accumulation of water vapour, thereby establishing the necessary conditions for cloud formation and hydrometeor development.

The spatio-temporal evolution of horizontal temperature advection (*HTA*) at 1000 hPa (Figs. A1a-d) clearly reveals that the Yellow Sea coastal region was initially dominated by pronounced low-level cold advection ($HTA < 0$). This persistent cold advection, acting through diabatic cooling effects, facilitated lower-tropospheric cooling and the maintenance of the inversion layer, thereby establishing a robust thermodynamic foundation for sea fog initiation. As the lifecycle progressed, this cold advection abated from the daytime of 15 May and gradually transitioned into weak warm advection or thermal neutrality by 00:00 UTC on 16 May (Fig. A1d), marking a regime shift in the atmospheric boundary layer (ABL) thermal structure from a predominantly cooling-driven process to a more complex, dynamically evolving state.

Concurrently, the moisture dynamic field (Figs. A1e-h) exhibits an evolutionary trajectory highly synergistic with the thermal field. While intense moisture convergence (negative *VIMD*) was primarily confined to the southern Yellow Sea during the daytime (Figs. A1e-f), a localized region of strong convergence developed rapidly along the coast during the nighttime mature stage (Fig. A1g). This robust dynamical forcing provided critical support for localized moisture accumulation, thereby ensuring an ample water vapour supply essential for the fog's maintenance and intensification (Fig. A1h). The synergistic evolution of thermal cooling and moisture convergence not only drove the rapid near-surface saturation and inversion intensification as discussed in Sect. 3.2, but also constituted the requisite large-scale environment for the downward grounding of low clouds and their subsequent transformation into sea fog.

Appendix B: Satellite-based identification of sea fog using FY-4B brightness temperature difference

The distribution and evolution of sea fog were identified using FY-4B geostationary satellite data provided by the National Satellite Meteorological Center (NSMC). Given the lack of solar reflectance during nocturnal periods, the brightness temperature difference (*BTD*) between the 10.8 µm (Channel 12) and 3.7 µm (Channel 8) bands of the FY-4B Advanced Geosynchronous Radiation Imager (AGRI) was employed. Channel 12 is situated within the atmospheric infrared window, providing sensitivity to cloud- and fog-top temperatures. In contrast, the emissivity of liquid water clouds at 3.7 µm is lower than that in the infrared window, resulting in higher brightness temperatures at 10.8 µm ($T_{10.8}$) than at 3.7 µm ($T_{3.7}$) for water clouds such as sea fog and stratus. Positive *BTD* values ($BTD = T_{10.8} - T_{3.7}$), typically ranging from 2 to 5 K, allow for the effective identification of low clouds and sea fog, whereas *BTD* values for clear-sky or ice-cloud regions are near zero or negative.

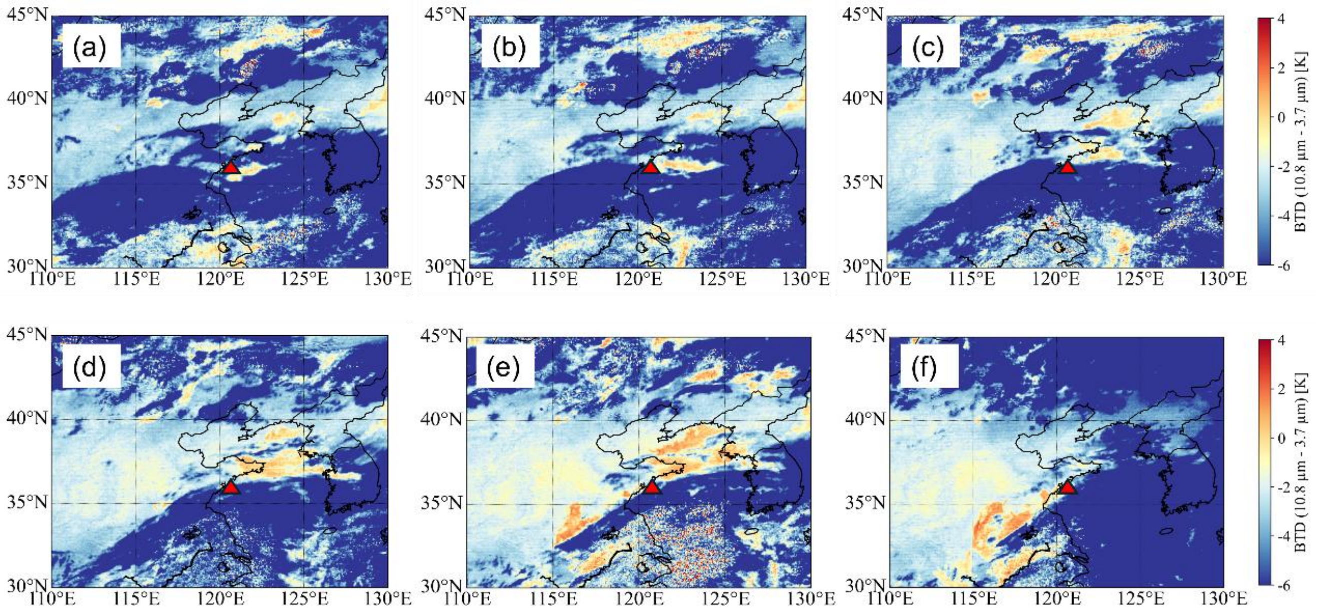

Figure B1. Distribution of the brightness temperature difference (BTD, T10.8-T3.7) from FY-4B at (a) 12:00 UTC (b) 14:00 UTC on 15 May; (c) 16:00 UTC, (d) 18:00 UTC (e) 20:00 UTC, and (f) 21:00 UTC on 16 May 2025.

Figure B1 depicts the temporal evolution of *BTD* signatures, capturing the distinct transitions across the formation, maintenance, and dissipation stages of the sea fog event. At 12:00-14:00 UTC on 15 May (Figs. B1a, b), a localized region of positive *BTD* was discernible over the Yellow Sea east of the Huangdao station, coinciding with the presence of low stratus. Driven by the prevailing onshore flow, the positive *BTD* signature underwent westward expansion and inland propagation, eventually overtaking the Huangdao station and adjacent coastal zones by 16:00 UTC (Fig. B1c). This spatial evolution directly synchronized with the decline in surface visibility to below 1 km, marking the onset of the sea fog. During the mature stage (18:00-20:00 UTC; Figs. B1d, e), the spatial footprint of the positive *BTD* signal reached its maximum extent. *BTD* values overlying the station and marine sectors remained consistently elevated and spatially homogeneous, signifying a structurally stable and horizontally uniform fog layer, which coincided with the minimum visibility observations (~100 m). By 21:00 UTC (Fig. B1f) , the *BTD* signal began to attenuate and contract, reflecting the lifting of the fog layer into low-level stratus and the subsequent recovery of surface visibility.

Appendix C: Ka-band cloud radar reflectivity during the stratus–fog–stratus transition

Based on the range height indicator (RHI) and plan position indicator (PPI) scans from a Ka-band cloud radar (center frequency: 35 GHz; wavelength: 8.6 mm) at the Huangdao Meteorological Bureau, we systematically analyzed the radar echo characteristics during the three-stage stratus–fog–stratus transition, integrated with surface visibility and meteorological observations.

https://doi.org/10.5194/egusphere-2026-3143
Preprint. Discussion started: 24 June 2026

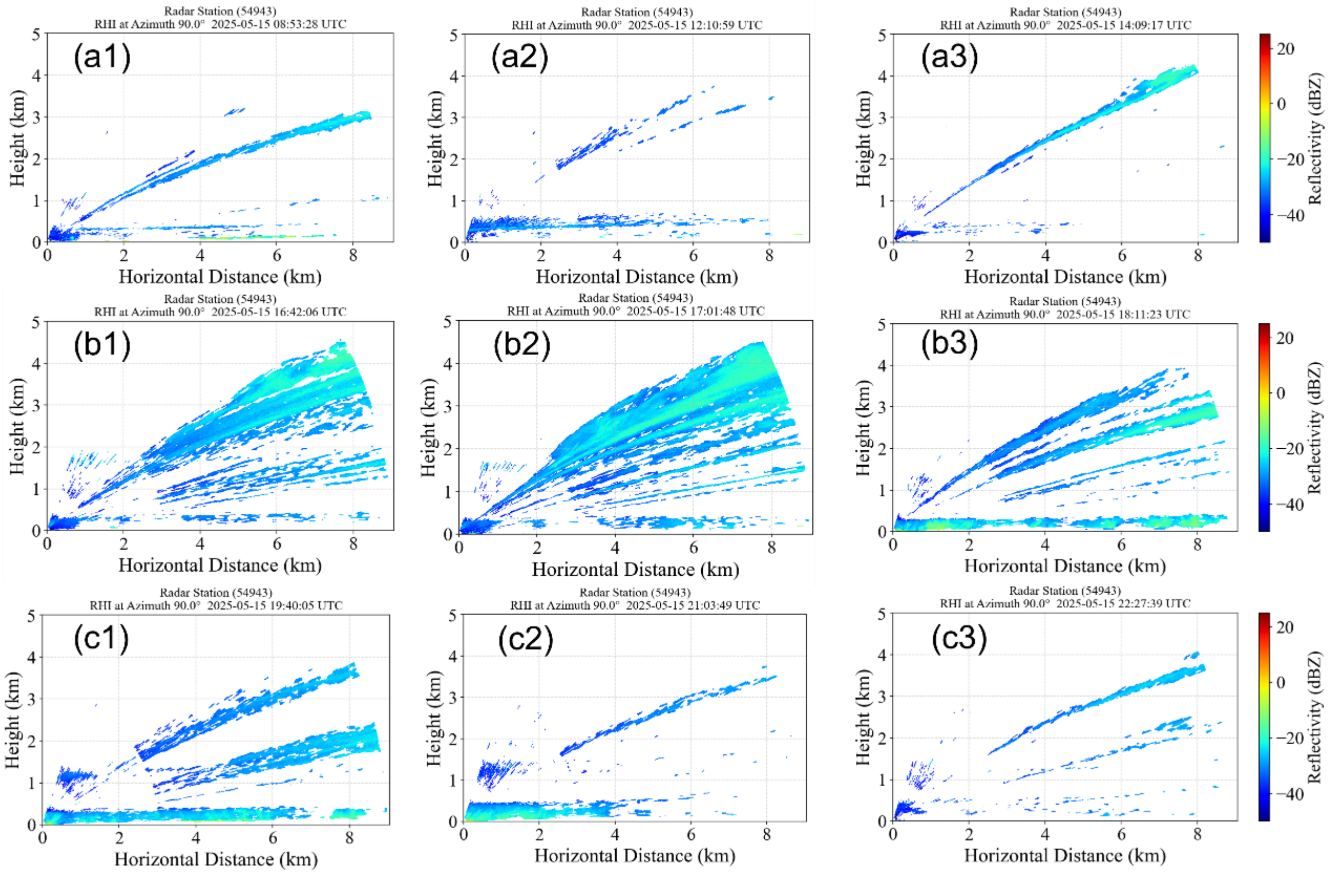

Figure C1. Vertical scans (RHI) from the Ka-band cloud radar at (a) 08:53, 12:10, 14:09 UTC; (b) 16:42, 17:01, 18:11 UTC (on 15 May); and (c) 19:40, 21:03, 22:27 UTC (on 15 May 2025). The scanning azimuth is 90°.

Figure C1 presents the RHI scan results. Prior to fog onset (Figs. C1a1-a3), the reflectivity cores were exclusively elevated, with the stratus base exhibiting a clear separation from the surface and an absence of surface-reaching echoes. The reflectivity factor (*Z*) was generally weak and characterized by discrete, inhomogeneous distributions with limited vertical development. The horizontal extent was small, and the structure lacked the homogeneous stratified features typically associated with robust turbulent mixing. During the active sea fog stages (Figs. C1b1-b3 and C1c1-c2), the radar echoes bridged the vertical gap between the overlying stratus and the surface, forming a continuous, surface-reaching reflectivity column. Reflectivity intensified significantly, displaying a homogeneous stratified structure indicative of vigorous turbulent mixing within the mature fog layer. The horizontal coverage expanded significantly with a stable echo thickness, reflecting a mature, fully developed fog layer. Following dissipation (Fig. C1c3), the surface-level echoes subsided, and the reflectivity layer re-ascended to become detached from the surface. The horizontal continuity decreased, returning to discrete, weak scattering characteristics consistent with the pre-fog stratus state.

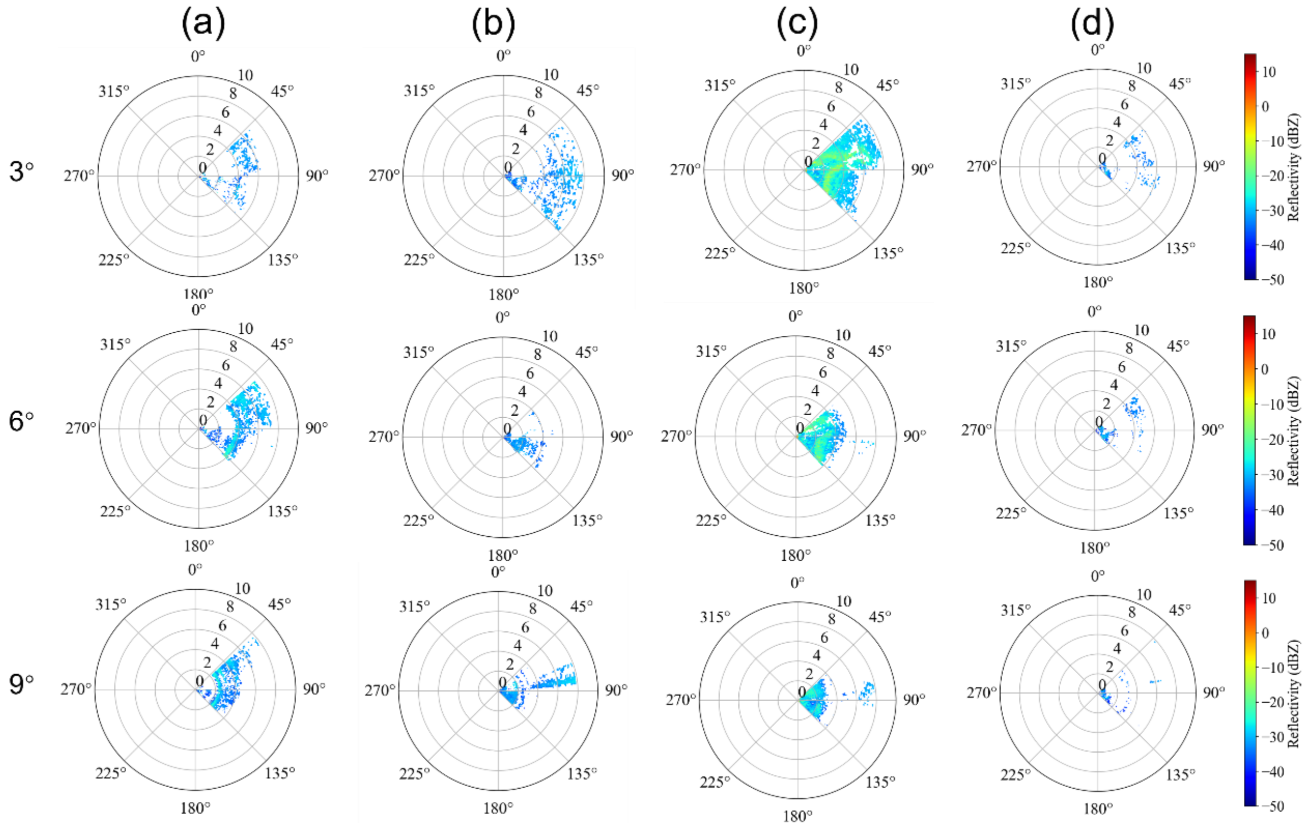

Figure C2. PPI scans within a specified azimuth range (48.17°-135.08°) at (a) 11:56 UTC on 15 May, (b) 16:00 UTC on 15 May, (c) 20:02 UTC on 15 May and (d) 23:04 UTC on 15 May. The rows from top to bottom correspond to elevation angles of 3°, 6°, 9°, respectively.

Figure C2 displays the PPI scans, illustrating the horizontal distribution of radar reflectivity during the fog evolution. At 11:56 UTC on 15 May (Fig. C2a), no radar returns were detected at the surface across all elevation angles (3°, 6°, 9°). The echoes appeared as discrete spots with limited coverage and weak intensity, corresponding to the pre-fog stratus stage. At 16:00 UTC on 15 May (Fig. C2b), surface-level echoes were present; however, reflectivity remained low and horizontally inhomogeneous. This is likely attributable to the limited vertical extent of the incipient fog layer-where the fog top resides below the radar's dead zone-and its spatially fragmented distribution. Subsequently (Fig. C2c), large-scale, uniform, and continuous sheet-like surface-reaching echoes appeared first at the 3° elevation angle, coinciding with a sharp reduction in surface visibility to approximately 100 m. Echoes at 6° and 9° also intensified and merged, indicating that the fog layer extended vertically to several hundred meters. The minimal spatial gradients and homogeneous reflectivity distribution align with the well-mixed nature of the mature sea fog. By 23:04 UTC on 15 May (Fig. C2d), reflectivity attenuated across all elevation angles, and the previous continuous sheet-like structures fragmented, coinciding with the loss of surface-reaching echoes and the transition of fog lifting into stratus. In summary, the Ka-band cloud radar successfully captured the three-stage evolution from stratus (elevated echoes, low reflectivity) to sea fog (surface-reaching echoes, increased intensity, uniform horizontal distribution) and back to stratus (echo lifting, attenuated reflectivity). These results exhibit high consistency with the vertical profiles from the UAV-borne LCPIS, surface visibility, and microphysical parameters (e.g., liquid water content and number concentration), providing robust evidence for the boundary-layer dynamics and microphysical mechanisms governing sea fog development and dissipation.

Code and data availability

The codes developed for this study are available from the corresponding author upon reasonable request (email: zengqingwei@nudt.edu.cn). The ERA5 reanalysis data, provided by the European Centre for Medium-Range Weather Forecasts (ECMWF), are accessible through the Copernicus Climate Data Store (https://cds.climate.copernicus.eu/datasets/reanalysis-era5-pressure-levels). Radiosonde measurements for Qingdao were obtained from the University of Wyoming Sounding Archive (http://weather.uwyo.edu/upperair/sounding.html). The FY-4B data were acquired from the National Satellite Meteorological Center of China (https://data.nsmc.org.cn/).

.

Author contributions

The author contributions are defined following the CRediT (Contributor Roles Taxonomy) framework. Qingwei Zeng conducted data analysis and drafted the original manuscript. Lei Liu and Xichuan Liu conceived the research idea and designed the overall study framework. Lele Cai and Qinghui Li developed and established the observational methodology. Hao Zhou undertook manuscript revision and polished the academic presentation. All co-authors participated in field observations and in-situ data collection, curated observational and multi-source datasets, performed result visualization, assisted with data processing and numerical validation, and provided valuable comments and revisions to improve the manuscript. All authors have read and fully approved the final submitted version of the manuscript.

Competing interests

The authors declare that they have no conflict of interest.

Acknowledgements

We acknowledge the European Centre for Medium-Range Weather Forecasts (ECMWF) for providing the ERA5 reanalysis data (https://cds.climate.copernicus.eu/). Furthermore, the field experiment received substantial support from the Qingdao

Institute of Marine Meteorology. The authors also thank Dongli Zhai, Dong Liu, and Tianwen Zhang from the Luoyang Branch of Beijing Juheng Bolian Technology Co. Ltd. for providing technical and experimental support.

Financial support

This research has been supported by the National Key R&D Program of China (grant no. 2021YFC2802501), Hunan Furong Youth Talent Project for Scientific and Technological Innovation (grant no. 2025RC3109), and the National Natural Science Foundation of China (grant no. 42105176).

Review statement

The review statement will be added by Copernicus Publications listing the handling editor as well as all contributing referees according to their status anonymous or identified.

References

Cai, L., Liu, L., Zeng, Q., and Wang, P.: Design and experiment of a lightweight cloud particle imager, Meas. Sci. Technol., 35, 115801, https://doi.org/10.1088/1361-6501/ad6b40, 2024.

Chambers, T. E., Reid, I. M., and Hamilton, M.: A lightweight holographic imager for cloud microphysical studies from an untethered balloon, Atmos. Meas. Tech., 17, 3237-3253, https://doi.org/10.5194/amt-17-3237-2024, 2024.

Costabloz, T., Burnet, F., Lac, C., Martinet, P., Delanoë, J., Jorquera, S., and Fathalli, M.: Vertical profiles of liquid water content in fog layers during the SOFOG3D experiment, Atmos. Chem. Phys., 25, 6539-6573, https://doi.org/10.5194/acp-25-6539-2025, 2025.

Dorman, C. E., Grachev, A. A., Gultepe, I., and Fernando, H. J. S.: Toward Improving Coastal-Fog Prediction (C-FOG), Bound.-Layer Meteorol., 181, 167-170, https://doi.org/10.1007/s10546-021-00664-8, 2021.

Egli, S., Maier, F., Bendix, J., and Thies, B.: Vertical distribution of microphysical properties in radiation fogs — A case study, Atmos. Res., 151, 130-145, https://doi.org/10.1016/j.atmosres.2014.05.027, 2015.

Fernando, H. J. S., Gultepe, I., Dorman, C., Pardyjak, E., Wang, Q., Hoch, S. W., Richter, D., Creegan, E., Gaberšek, S., Bullock, T., Hocut, C., Chang, R., Alappattu, D., Dimitrova, R., Flagg, D., Grachev, A., Krishnamurthy, R., Singh, D. K., Lozovatsky, I., Nagare, B., Sharma, A., Wagh, S., Wainwright, C., Wroblewski, M., Yamaguchi, R., Bardoel, S., Coppersmith, R. S., Chisholm, N., Gonzalez, E., Gunawardena, N., Hyde, O., Morrison, T., Olson, A., Perelet, A., Perrie, W., Wang, S., and Wauer, B.: C-FOG: Life of Coastal Fog, Bull. Amer. Meteor. Soc., 102, E244-E272, https://doi.org/10.1175/BAMS-D-19-0070.1, 2021.

Fernando, H. J. S., Dorman, C., Pardyjak, E., Shen, L., Wang, Q., Creegan, E., Gaberšek, S., Gultepe, I., Hoch, S., Lenain, L., Richter, D., Chang, R., VandenBoer, T. C., Bardoel, S., Barve, A., Blomquist, B., Bullock, T., Chen, Z., Colosi, L., Coppersmith, R. S., Crawford, I., Crilley, L. R., Dimitrova, R., Dowling, A., Eleuterio, D., Fiorino, S., Gallagher, M., Gapp, N., Giacosa, G., Grachev, A., Grare, L., Hintz, T., Hocut, C., Huang, K. Y., Hyde, O., Keefer, K., Ortiz-Suslow, D. G., Perelet, A., Perrie, W., Ruiz-Plancarte, J., Salehpoor, L., Singh, D., Statom, N., Taylor, P., Wang, S., and Yamaguchi, R.: Fatima-GB: Searching Clarity within Marine Fog, Bull. Amer. Meteor. Soc., 106, E971-E1016, https://doi.org/10.1175/BAMS-D-23-0050.1, 2025.

Fu, G., Guo, J., Pendergrass, A., and Li, P.: An analysis and modeling study of a sea fog event over the Yellow and Bohai Seas, J. Ocean Univ. China, 7, 27-34, https://doi.org/10.1007/s11802-008-0027-z, 2008.

Fuchs, C., Ramelli, F., Schweizer, D., Lohmann, U., and Henneberger, J.: Putting the spotlight on small cloud droplets with SmHOLIMO – a new holographic imager for in situ measurements of clouds, Atmos. Meas. Tech., 18, 2969–2986, https://doi.org/10.5194/amt-18-2969-2025, 2025.

Girdwood, J., Smith, H., Stanley, W., Ulanowski, Z., Stopford, C., Chemel, C., Doulgeris, K.-M., Brus, D., Campbell, D., and Mackenzie, R.: Design and field campaign validation of a multi-rotor unmanned aerial vehicle and optical particle counter, Atmos. Meas. Tech., 13, 6613-6630, https://doi.org/10.5194/amt-13-6613-2020, 2020.

Goodman, J.: The Microstructure of California Coastal Fog and Stratus, J. Appl. Meteor. Climatol., 16, 1056-1067, https://doi.org/10.1175/1520-0450(1977)016%3C1056:TMOCCF%3E2.0.CO;2, 1977.

Gultepe, I., Tardif, R., Michaelides, S. C., Cermak, J., Bott, A., Bendix, J., Müller, M. D., Pagowski, M., Hansen, B., Ellrod, G., Jacobs, W., Toth, G., and Cober, S. G.: Fog Research: A Review of Past Achievements and Future Perspectives, Pure Appl. Geophys., 164, 1121-1159, https://doi.org/10.1007/s00024-007-0211-x, 2007.

Gultepe, I., Sharman, R., Williams, P. D., Zhou, B., Ellrod, G., Minnis, P., Trier, S., Griffin, S., Yum, Seong. S., Gharabaghi, B., Feltz, W., Temimi, M., Pu, Z., Storer, L. N., Kneringer, P., Weston, M. J., Chuang, H., Thobois, L., Dimri, A. P., Dietz, S. J., França, G. B., Almeida, M. V., and Neto, F. L. A.: A Review of High Impact Weather for Aviation Meteorology, Pure Appl. Geophys., 176, 1869-1921, https://doi.org/10.1007/s00024-019-02168-6, 2019.

Guo, J., Xu, J., and Xu, X.: An observational and modeling study of a sea fog event over the yellow and east China seas on 17 March 2014, Trop. Cyclone Res. Rev., 10, 182-190, https://doi.org/10.1016/j.tcrr.2021.09.001, 2021.

Kaikkonen, V. A., Molkoselkä, E. O., Juttula, H. J., and Mäkynen, A. J.: UAV Cloud Particle Sensor, in: 2024 IEEE International Instrumentation and Measurement Technology Conference (I2MTC), 2024 IEEE International Instrumentation and Measurement Technology Conference (I2MTC), 1-6, https://doi.org/10.1109/I2MTC60896.2024.10560651, 2024.

Koračin, D., Lewis, J., Thompson, W. T., Dorman, C. E., and Businger, J. A.: Transition of Stratus into Fog along the California Coast: Observations and Modeling, J. Atmos. Sci., 58, 1714-1731, https://doi.org/10.1175/1520-0469(2001)058%3C1714:TOSIFA%3E2.0.CO;2, 2001.

Koračin, D., Dorman, C. E., Lewis, J. M., Hudson, J. G., Wilcox, E. M., and Torregrosa, A.: Marine fog: A review, Atmos. Res., 143, 142-175, https://doi.org/10.1016/j.atmosres.2013.12.012, 2014.

Lewis, J. M., Koračin, D., and Redmond, K. T.: Sea Fog Research in the United Kingdom and United States: A Historical Essay Including Outlook, Bull. Amer. Meteor. Soc., 85, 395-408, https://doi.org/10.1175/BAMS-85-3-395, 2004.

Liu, J.-W., Sun, Y., and Yang, L.: Interannual Variability in Summertime Sea Fog Over the Northern Yellow Sea and Its Association With the Local Sea Surface Temperature, J. Geophys. Res. Atmos., 126, e2020JD034439, https://doi.org/10.1029/2020JD034439, 2021.

Ming, H., Wei, M., Wang, M., Gao, L., Chen, L., and Wang, X.: Analysis of fog at Xianyang Airport based on multi-source ground-based detection data, Atmos. Res., 220, 34-45, https://doi.org/10.1016/j.atmosres.2019.01.012, 2019.

Oliver, D. A., Lewellen, W. S., and Williamson, G. G.: The Interaction between Turbulent and Radiative Transport in the Development of Fog and Low-Level Stratus, J. Atmos. Sci., 35, 301-316, https://doi.org/10.1175/1520-0469(1978)035%3C0301:TIBTAR%3E2.0.CO;2, 1978.

Pilié, R. J., Mack, E. J., Rogers, C. W., Katz, U., and Kocmond, W. C.: The Formation of Marine Fog and the Development of Fog-Stratus Systems along the California Coast, J. Appl. Meteor. Climatol., 18, 1275-1286, https://doi.org/10.1175/1520-0450(1979)018%3C1275:TFOMFA%3E2.0.CO;2, 1979.

Pope, N. H. and Igel, A. L.: Counteracting influences of gravitational settling modulate aerosol impacts on cloud-base-lowering fog characteristics, Atmos. Chem. Phys., 25, 5433–5444, https://doi.org/10.5194/acp-25-5433-2025, 2025.

Price, J., Porson, A., and Lock, A.: An Observational Case Study of Persistent Fog and Comparison with an Ensemble Forecast Model, Boundary-Layer Meteorol, 155, 301-327, https://doi.org/10.1007/s10546-014-9995-2, 2015.

Rabbath, C. A. and Corriveau, D.: A comparison of piecewise cubic Hermite interpolating polynomials, cubic splines and piecewise linear functions for the approximation of projectile aerodynamics, Defence Technology, 15, 741-757, https://doi.org/10.1016/j.dt.2019.07.016, 2019.

Ramelli, F., Beck, A., Henneberger, J., and Lohmann, U.: Using a holographic imager on a tethered balloon system for microphysical observations of boundary layer clouds, Atmos. Meas. Tech., 13, 925-939, https://doi.org/10.5194/amt-13-925-2020, 2020.

Singh, D. K., Hoch, S. W., Gultepe, I., and Pardyjak, E. R.: A case study of the life cycle of a stratus-lowering coastal-fog event in Newfoundland, Canada, Q. J. Roy. Meteor. Soc., 150, 641-662, https://doi.org/10.1002/qj.4615, 2024.

Taylor, P. A., Chen, Z., Cheng, L., Afsharian, S., Weng, W., Isaac, G. A., Bullock, T. W., and Chen, Y.: Surface deposition of marine fog and its treatment in the Weather Research and Forecasting (WRF) model, Atmos. Chem. Phys., 21, 14687-14702, https://doi.org/10.5194/acp-21-14687-2021, 2021.

Torregrosa, A., O'Brien, T. A., and Faloona, I. C.: Coastal Fog, Climate Change, and the Environment, Eos, Transactions American Geophysical Union, 95, 473-474, https://doi.org/10.1002/2014EO500001, 2014.

Wan, J., Su, J., Sheng, H., Liu, S., and Li, J.: Spatial and Temporal Characteristics of Sea Fog in Yellow Sea and Bohai Sea Based on Active and Passive Remote Sensing, in: IGARSS 2020 - 2020 IEEE International Geoscience and Remote Sensing Symposium, IGARSS 2020 - 2020 IEEE International Geoscience and Remote Sensing Symposium, 5477-5480, https://doi.org/10.1109/IGARSS39084.2020.9324028, 2020.

Yang, L., Liu, J.-W., Xie, S.-P., and Shen, S. S. P.: Transition from Fog to Stratus over the Northwest Pacific Ocean: Large-eddy Simulation, Mon. Weather Rev., 149, 2913-2925, https://doi.org/10.1175/MWR-D-20-0420.1, 2021.